INTERNATIONAL JOURNAL FOR NUMERICAL METHODS IN ENGINEERING
Int. J. Numer. Meth. Engng 2004; **60/5**:1–38 *Prepared using* nmeauth.cls *[Version: 2002/09/18 v2.02]*

A stabilized volume-averaging finite element method for flow in porous media and binary alloy solidification processes

Nicholas Zabaras*† and Deep Samanta

Materials Process Design and Control Laboratory, Sibley School of Mechanical and Aerospace Engineering, 188 Frank H. T. Rhodes Hall, Cornell University, Ithaca, NY 14853-3801, U.S.A

SUMMARY

A stabilized equal-order velocity-pressure finite element algorithm is presented for the analysis of flow in porous media and in the solidification of binary alloys. The adopted governing macroscopic conservation equations of momentum, energy and species transport are derived from their microscopic counterparts using the volume-averaging method. The analysis is performed in a single-domain with a fixed numerical grid. The fluid flow scheme developed includes SUPG (streamline-upwind/Petrov-Galerkin), PSPG (pressure stabilizing/Petrov-Galerkin) and DSPG (Darcy stabilizing/Petrov-Galerkin) stabilization terms in a variable porosity medium. For the energy and species equations a classical SUPG-based finite element method is employed. The developed algorithms were tested extensively with bilinear elements and were shown to perform stably and with nearly quadratic convergence in high Rayleigh number flows in varying porosity media. Examples are shown in natural and double diffusive convection in porous media and in the directional solidification of a binary-alloy.

KEY WORDS: Stabilized finite element method; volume averaging; Darcy flows; porous media; convection; solidification

1. INTRODUCTION

The understanding of metal alloy solidification processes is essential in many industrial applications such as casting, welding and growth of single crystals. Most alloys solidify with the

*Correspondence to: Nicholas Zabaras, Materials Process Design and Control Laboratory, Sibley School of Mechanical and Aerospace Engineering, 188 Frank H. T. Rhodes Hall, Cornell University, Ithaca, NY 14853-3801, U.S.A
†Email: zabaras@cornell.edu

Contract/grant sponsor: NASA Physical Sciences Division, Materials Science Program; contract/grant number: 98-HEDS-05

Contract/grant sponsor: University-Industry Partnerships for Aluminum Industry of the Future Program of the Office of Industrial Technologies of the U.S. Department of Energy; contract/grant number: DE-FC07-02ID14396

Received 26 March 2003
Revised 23 June 2003
Accepted 10 September 2003

formation of a two phase region known as mushy zone, which is composed of solid dendrites and interdendritic liquid. The morphology and size of the resulting solidification microstructure and the properties of cast products depend on many factors including the convection in the melt and mushy region during solidification. The most common causes of fluid flow in alloy solidification are thermal and solutal gradients, surface tension gradients, shrinkage and external forcing agents such as rotation, vibration, electromagnetic fields, etc. We are herein interested to develop a finite element methodology for the analysis of flow in variable porosity porous media. Such flows constitute typical mechanisms usually employed in the solidification of alloys.

The difficulty associated with the modeling of solidification processes arises from the morphological complexity of the resulting microstructure and the variety of length- and time-scales in the system. Figure 1 shows two typical length-scales and some of the corresponding physical phenomena that are involved in solidification. At the macroscopic scale, fluid flow, convective-conductive heat transfer, macrosegregation, solid movement and deformation are some of the mechanisms present. At the microscopic scale, interdendritic flow due to shrinkage, latent heat release due to phase change, nucleation and microstructure formation mechanisms are present. Other scales also exist in the solidification process, such as the solute diffusion length scale and the capillary length scale [1, 2].

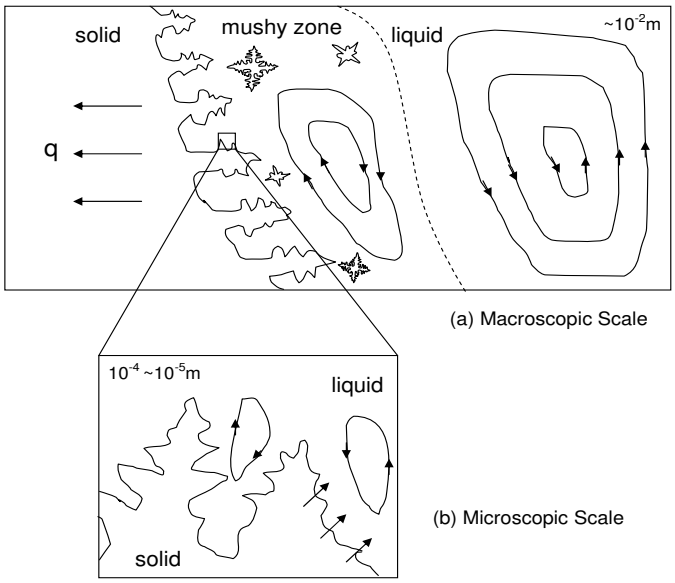

Figure 1. Different length-scales in a typical solidification process with a schematic of various convection patterns [2].

In this paper, we are only interested in single-domain solidification models based on volume averaging and other approaches are not discussed. Single-domain models, which overcome many of the limitations of multidomain methods (e.g. of front-tracking methods [3]), emerged in the mid-1980s [4, 5] and showed promise of becoming useful tools for simulating solidification processes. These models consist of a single set of equations for momentum, energy and species transport in multi-constituent, solid-liquid, phase change systems, which concurrently are

applied in all regions (solid, mushy and liquid). They require only a single, fixed numerical grid and a single set of boundary conditions to compute the solution. This brings a significant advantage in the numerical solution as there is no need to track the boundaries between phases. Instead, the interfaces are implicitly defined by the distributions of energy and composition determined from the solutions of the model equations (i.e. as post-processing operations). The momentum equations are a generalization of Darcy' law and reduce to the single-phase Navier-Stokes equations in the liquid region.

Some of the earliest continuum models for binary alloy solidification used classical mixture theory to postulate macroscopic equations without reference to any microscopic equations [6]-[8]. A similar mathematical model in which, however, the macroscopic transport equations were derived from the classical microscopic transport equations using volume-averaging is presented in [9]. Models have also been presented in which the conservation equations for each phase are solved separately with the aid of interphase transport models [10, 11]. Other developments in this direction can be found in [12]-[16].

In terms of numerical implementation of the single domain model, almost all the reported algorithms have been implemented by the finite difference method [8, 7, 11]. Some finite element implementations have also been developed but their applicability seems limited in accurately modeling solidification phenomena at high Rayleigh number melt flows or in accurately predicting the pressure distribution in the mushy zone. Among these methods, we refer to the penalty method (see [17]) implementation of Poirier, Heinrich and colleagues [18, 19] and the fractional step method [20] implemented by Nithiarasu et al. mostly for natural and double-diffusive convection in porous media flows [21, 22]. As part of our continuing efforts for the development of a robust simulator for solidification processes, we have implemented and tested both of these methods.

Stabilized finite element calculations for volume-averaging based solidification models have not been reported earlier. Even though SUPG/PSPG stabilization techniques [23]-[25] can be useful in such models, their implementation shows that they alone cannot capture the underlying phenomena especially for variable porosity as is the case in modeling flow in the mushy zone. In a very recent work, Masud and Hughes proposed stabilization terms for pure Darcy flow [26] that work well without mesh-dependent parameters. We will present a stabilized FEM for the generalized Navier Stokes/Darcy equations in varying porosity porous media flows and solidification systems. In addition to the selection of the stabilization terms, other key ingredients of the developed approach include the overall numerical scheme coupling the flow, heat and species transport, the solution of the assembled equations and the required updates for the phase change process.

The organization of the paper is as follows. In Section 2, a brief review of the mathematical volume-averaging formulation considered here together with the required closure relationships is presented. Section 3 provides the final dimensionless form of the mathematical model considered for modeling double-diffusive convection in porous media. The overall thermodynamic relations and update formulae for the phase change process are summarized in Section 4. Section 5 presents the stabilized finite element formulation. The solution of the heat and species equations is summarized in Section 6. The summary of the coupling algorithm for the time integration of all sub-problems is given in Section 7. Numerical examples are summarized in Section 8. They include double diffusion convection in a cavity with uniform porosity, natural convection in a cavity with variable porosity and solidification of a binary mixture of ammonium-chloride and water at Ra=10^7.

2. VOLUME-AVERAGING MACROSCOPIC TRANSPORT EQUATIONS

In this work, we consider a two-component, two-phase (solid and liquid) binary alloy system. The macroscopic transport equations can be obtained by averaging the microscopic transport equations over a finite size control volume that contains both phases. The averaging volume is defined such that the scale it represents is small enough to capture the global fluid flow motion, heat transfer, and species distribution, but large enough to smooth out the details of the morphological complexities, interdendritic fluid flow, latent heat release and species redistribution. For such systems, for example in solidification processes, the averaging volume can track the overall nature of the liquid, solid and mushy regions without accounting for any details of the solidification microstructures. Under typical solidification conditions, the system and interfacial structures are of the orders of 10^{-1} to 10^{0} m and 10^{-5} to 10^{-4} m, respectively, so the size of the averaging volume in solidification can vary between 10^{-3} to 10^{-2} m. The resulting averaged transport equations need to be supplemented by constitutive relations that describe morphological characteristics and the interactions between the two phases.

The volume-averaging technique shows how various terms in the macroscopic equations arise and how the resulting macroscopic variables are related to the corresponding microscopic variables [27]. This gives considerable insight into the formulation of constitutive relations and holds the key for incorporating the evolution of the solid structure and transport phenomena at the micro level into a macroscopic model.

The microscopic (exact) mass, momentum, energy and species transport equations for phase k (here $k = s, l$) are given by:

$$Mass \qquad \frac{\partial \rho_k}{\partial t} + \nabla \cdot (\rho_k \boldsymbol{v}_k) = 0 \tag{1}$$

$$Momentum \qquad \frac{\partial \rho_k \boldsymbol{v}_k}{\partial t} + \nabla \cdot (\rho_k \boldsymbol{v}_k \boldsymbol{v}_k) = \nabla \cdot \boldsymbol{\sigma}_k + \mathbf{b}_k \tag{2}$$

$$Energy \qquad \frac{\partial \rho_k h_k}{\partial t} + \nabla \cdot (\rho_k h_k \boldsymbol{v}_k) = -\nabla \cdot \mathbf{q}_k \tag{3}$$

$$Species \qquad \frac{\partial \rho_k C_k}{\partial t} + \nabla \cdot (\rho_k C_k \boldsymbol{v}_k) = -\nabla \cdot \mathbf{j}_k \tag{4}$$

where $\boldsymbol{\sigma}$ is the stress tensor, $\mathbf{b}$ is the body force, $\mathbf{q}$ is the heat flux, $\mathbf{j}$ is the species diffusion flux and the rest of the notation is standard. The detailed expressions for these terms are supplied by constitutive equations for specific cases. The energy equation is here written in terms of the total enthalpy. For simplicity, viscous heat dissipation, compression work, and volumetric energy and species sources are not included. One can easily relax these assumptions as required.

The equations above representing microscopic transport in each phase k take the general form:

$$\frac{\partial \Phi_k}{\partial t} + \nabla \cdot (\Phi_k \ \boldsymbol{v}_k) = \nabla \cdot \mathbf{J}_k + S_k \tag{5}$$

for appropriate selection of the fields $\Phi, \mathbf{J}$ and S.

In order to provide some physical insight of the mathematical models examined in this paper, we herein provide a brief review of the foundations of volume-averaging techniques and for more details the reader can consult references [27]-[29]. Let us introduce the phase function ν_k taking the value 1 in phase k and zero elsewhere. We can then define the volume fraction ϵ_k of phase k as follows:

$$\epsilon_k = \frac{1}{dV}\int_{dV} \nu_k(\boldsymbol{x},t)dv = dV_k/dV \tag{6}$$

where dV_k is the portion of dV that is occupied by phase k.

The volume-averaged quantity $< \Psi_k >$ of any quantity $\Psi(\boldsymbol{x},t)$ in phase k over the entire averaging volume dV can now be introduced as:

$$< \Psi_k >= \frac{1}{dV}\int_{dV} \Psi_k \nu_k(\boldsymbol{x},t)dv \tag{7}$$

Similarly, one can introduce the intrinsic volume-averaged quantity $< \Psi_k >^k$ (averaged value of $\Psi(\boldsymbol{x},t)$ in the control volume dV_k) as:

$$< \Psi_k >^k= \frac{1}{dV_k}\int_{dV} \Psi_k \nu_k(\boldsymbol{x},t)dv = \frac{< \Psi_k >}{\epsilon_k} \tag{8}$$

When Ψ_k is uniformly distributed in dV_k, then $< \Psi_k >^k= \Psi_k$.

The fluctuating component $\hat{\Psi}_k$ is commonly introduced to represent the deviation of Ψ_k from the intrinsic volume-averaged $< \Psi_k >^k$. It is given by:

$$\hat{\Psi}_k = (\Psi_k - < \Psi_k >^k)\nu_k \tag{9}$$

In phase k, $\hat{\Psi}_k$ is zero only when Ψ_k is uniformly distributed.

Various volume-averaging formulae important to transport phenomena have been derived in [30]-[33]. They include, for example, a relation for the average of a product of two fields, the average of the time derivative in terms of the time derivative of the average, the average of the spatial derivative in terms of the spatial derivative of the average, etc.

Multiplying each side of Equation (5) representing microscopic transport by ν_k, integrating it over the averaging volume dV and applying averaging formulae such as the ones mentioned above, we obtain the following macroscopic transport equation for phase k:

$$\begin{aligned}\frac{\partial < \Phi_k >}{\partial t} + \nabla\cdot\epsilon_k < \Phi_k >^k < \boldsymbol{v}_k >^k = \nabla\cdot < \mathbf{J}_k > + < S_k > \\ +\nabla\cdot\frac{1}{dV}\int_{dV}(-\widehat{\Phi_k}\widehat{\boldsymbol{v}_k})dv + \frac{1}{dV}\int_{dA_k}\mathbf{J}_k\cdot\boldsymbol{n}_k dA \\ +\frac{1}{dV}\int_{dA_k}\Phi_k(\boldsymbol{w}_k-\boldsymbol{v}_k)\cdot\boldsymbol{n}_k dA\end{aligned} \tag{10}$$

where dA_k is the interfacial area of phase k with the other phase, $\boldsymbol{n}$ is the outward unit normal of the infinitesimal element of area dA of phase k, and $\boldsymbol{w}$ is the velocity of the microscopic interface.

Compared with the exact microscopic equations (5), three extra terms I_k^D, I_k^J and I_k^Q appear from the volume averaging procedure of the form:

$$I_k^D \equiv \nabla\cdot\frac{1}{dV}\int_{dV}(-\widehat{\Phi_k}\widehat{\boldsymbol{v}_k})dv \tag{11}$$

$$I_k^J \equiv \frac{1}{dV}\int_{dA_k}\mathbf{J}_k\cdot\boldsymbol{n}_k dA \tag{12}$$

$$I_k^Q \equiv \frac{1}{dV}\int_{dA_k}\Phi_k(\boldsymbol{w}_k-\boldsymbol{v}_k)\cdot\boldsymbol{n}_k dA \tag{13}$$

At the microscopic scale characterizing the two phase region (e.g. the mushy zone in solidification processes), there always exist species, temperature, and velocity gradients in the liquid. Despite this fact, almost all models reported in the literature neglect the I_k^D term [6, 32, 33]. The same approximation is considered here as well. The term I_k^Q accounts for the interfacial transfer due to phase change, whereas I_k^J represents the transport phenomena between phases within dV by diffusion and is related to the gradients of microscopic velocity, temperature and species concentration on each side of the solid/liquid interface dA_k [11].

In this work, the averaged macroscopic equations from different phases are added within the averaging volume dV, therefore, detailed modeling of the interfacial transfer terms I_k^J and I_k^Q can be avoided. The heat or mass lost from one phase is gained by other phases, i.e.

$$\sum_k I_k^J = 0 \qquad and \qquad \sum_k I_k^Q = 0 \tag{14}$$

The model discussed here is unsuitable for modeling interfacial behavior. Interfacial phenomena can be modeled with the help of two phase models that involve detailed balance of interfacial fluxes between individual phases [11, 33].

In the following section, we will utilize this model in a single fixed domain and present the averaged macroscopic equations of mass, momentum, heat and species in the context of a general double-diffusive flow in a porous medium. Enhancement of this model to allow modeling of binary alloy solidification is provided in Section 4. Detailed discussion on more general volume averaging models is provided, for example, in [2], [34].

3. MATHEMATICAL MODEL FOR DOUBLE-DIFFUSIVE CONVECTION IN A FLUID-SATURATED POROUS MEDIUM

The volume averaging techniques developed in the earlier section are herein applied to the analysis of double-diffusive convective flow and of the associated heat and mass transfer in a fluid-saturated porous medium. To arrive at a model tractable for computation, we assume that only the solid and liquid phases may be present, that is, $\epsilon_l + \epsilon_s = 1$. In addition, the variations of material properties in dV_k are neglected, although globally they may vary, that is

Assumption 1: $< \rho_k >^k = \rho_k, \quad < \mu_k >^k = \mu_k, \quad < k_k >^k = k_k, \quad < D_l >^l = D_l, \quad D_s = 0,$ the last condition implying negligible species (solutal) diffusion in the solid phase.

Assumption 2: All phases in the averaging volume are assumed to be in thermodynamic equilibrium, i.e. $< T_s >^s = < T_l >^l$ and the liquid in the averaging volume is solutally well mixed, that is, $< C_l >^l = C_l$.

For the derivation of the macroscopic equation of mass conservation using Equation (10), we substitute $\Phi = \rho$, $\mathbf{J} = 0$, and $S = 0$. By writing and adding the individual macroscopic mass conservation equations for the two phases, neglecting the microscopic deviation term and considering the interfacial mass flux balance, i.e. $I_l^Q + I_s^Q = 0$, and the conditions of Assumption 1, we obtain:

$$\frac{\partial \rho}{\partial t} + \nabla \cdot (\rho \boldsymbol{v}) \ = 0 \tag{15}$$

where we have further defined:

$$\rho = \epsilon_l \, \rho_l + \epsilon_s \, \rho_s \tag{16}$$

$$\boldsymbol{v} = f_l < \boldsymbol{v}_l >^l = \frac{\rho_l}{\rho} \epsilon_l < \boldsymbol{v}_l >^l \tag{17}$$

where f_k $(k = s, l)$ denotes mass fraction of phase k, i.e. $\rho f_k = \rho_k \epsilon_k$.

Assumption 3: Note that we have assumed that $< \boldsymbol{v}_s >^s = 0$. In the context of solidification processes, such assumption for example will be appropriate for columnar but not equiaxed growth.

For deriving the macroscopic equation of momentum conservation from Equation (10), we take $\Phi = \rho \boldsymbol{v}$ and $S = \mathbf{b}$. Furthermore, we assume a Newtonian fluid and hence the viscous-stress in terms of the rate of deformation is given as,

$$\boldsymbol{\sigma} = -p_l I + \mu_l [\nabla \boldsymbol{v}_l + (\nabla \boldsymbol{v}_l)^T]$$

As discussed earlier, we consider that $I_l^D = I_s^D = 0$ and approximate $< \mu_l >^l = \mu_l$. The interfacial momentum fluxes due to solidification balance each other, that is, $I_l^Q + I_s^Q = 0$. However, $I_l^J + I_s^J = \sigma \chi$, where σ is the surface tension, assumed to be constant, and χ is the mean curvature of the interface.

Flow through a mushy zone consisting of a continuous solid structure (here assumed as columnar dendritic crystals), is usually very slow due to the high value of the interfacial area concentration. Therefore, the dissipative interfacial stress may be modeled in analogy with Darcy law as follows:

$$I_l^J = -\frac{\epsilon_l^2 \, \mu_l \, < \boldsymbol{v}_l >^l}{K(\epsilon_l)} \tag{18}$$

where $K(\epsilon_l)$ is the permeability of the mushy zone. Values of the permeability have been reported for a columnar dendritic structure in the literature [35]. The permeability is commonly approximated using the Kozeny-Carman equation:

$$K(\epsilon_l) = \frac{K_0 \, \epsilon_l^3}{(1 - \epsilon_l)^2} \tag{19}$$

where K_0 is a permeability constant depending on the morphology of the two-phase mushy region.

Using the previous assumptions and the definition of ρ and $\boldsymbol{v}$ given earlier, the final form of the macroscopic transport equation of momentum conservation then yields:

$$\begin{aligned} \frac{\partial(\rho \, \boldsymbol{v})}{\partial t} + \nabla \cdot (\rho \frac{\boldsymbol{v}\boldsymbol{v}}{f_l}) = & - \epsilon_l \nabla < p_l >^l + \nabla \cdot \left[\mu_l \left(\nabla \left(\frac{\rho}{\rho_l} \boldsymbol{v} \right) + \left(\nabla \left(\frac{\rho}{\rho_l} \boldsymbol{v} \right) \right)^T \right) \right] \\ & - \epsilon_l \mu_l \frac{\rho}{\rho_l} \frac{\boldsymbol{v}}{K(\epsilon_l)} + \epsilon_l \rho_l \mathbf{g} \end{aligned} \tag{20}$$

where $\mathbf{g}$ is the gravity vector.

The change in liquid density is here expressed using the Boussinesq approximation $\rho_l = \rho_0[(1 - \beta_c(C - C_e) - \beta_T(T - T_e)]$ and it appears only in the body force term. The term

$-\epsilon_l \nabla < p_l >^l$ in Equation (20) is written as follows:

$$-\epsilon_l \nabla < p_l >^l = -\nabla < p_l > + \frac{< p_l >}{\epsilon_l} \nabla \epsilon_l \tag{21}$$

This modification is better suited for CFD applications with the second term on the right hand side treated as a source term.

For deriving the macroscopic equation of energy conservation we take $\Phi = \rho h$, where h represents the total enthalpy. In addition, we consider $S = 0$ and utilize Fourier's law $\mathbf{J} = -k\nabla T$. We also define the following:

$$\rho h = \rho_l \epsilon_l < h_l >^l + \rho_s \epsilon_s < h_s >^s \tag{22}$$

$$k^* = \epsilon_l k_l + \epsilon_s k_s \tag{23}$$

Equation (10) then yields the following:

$$\frac{\partial(\rho h)}{\partial t} + \nabla \cdot (\rho < h_l >^l \boldsymbol{v}) = \nabla \cdot (k^* \nabla T) \tag{24}$$

For arriving at the macroscopic equation of species conservation, we note that for this case, $\Phi = \rho C$, where C represents solutal concentration (per unit mass) and $S = 0$. Furthermore, we utilize Fick's law for species diffusion flux, that is, $\mathbf{J} = -\rho D \nabla C$. The macroscopic transport equation of species conservation can be derived from Equation (10) as follows:

$$\frac{\partial(\rho C)}{\partial t} + \nabla \cdot (\rho < C_l >^l \boldsymbol{v}) = \nabla \cdot (\rho_l D^* \nabla < C_l >^l) \tag{25}$$

where

$$\rho C = \rho_l \epsilon_l < C_l >^l + \rho_s \epsilon_s < C_s >^s \tag{26}$$

$$D^* = \epsilon_l D_l \tag{27}$$

Assumption 4: To further simplify the above equations, we will assume that the densities of the two phases are constant and equal, i.e. $< \rho_s >^s = \rho_s = \rho_l = < \rho_l >^l = \rho = \rho_0$, thus $f_s = \epsilon_s$ and $f_l = \epsilon_l$. In the context of solidification, such an assumption will imply no solidification-induced shrinkage.

We now non-dimensionalize our governing equations with the non-dimensional parameters being defined as

$$\hat{x} = \frac{x}{L}, \qquad \hat{t} = \frac{\alpha_l t}{L^2}, \qquad \hat{v} = \frac{v}{\alpha_l / L}, \qquad \hat{p} = \frac{p L^2}{\rho_0 \alpha_l^2}$$

$$\theta = \frac{T - T_e}{\Delta T}, \qquad \hat{C} = \frac{C - C_e}{\Delta C}, \quad \hat{h} = \frac{h}{c_l \Delta T}, \quad \hat{h}_f = \frac{h_f}{c_l \Delta T} \tag{28}$$

where ρ_o is a reference density, α_l the fluid thermal diffusivity, L a characteristic length and T_e, $\Delta T = T_0 - T_e$ and C_e, $\Delta C = C_0 - C_e$ are problem dependent characteristic values and increments in T and C, respectively. The important non-dimensional parameters are expressed in Table I.

We next finalize the dimensionless form of our double-diffusive convection model of a two phase (solid/liquid) dilute, incompressible binary mixture. The mixture is confined in mass

Table I. Dimensionless groups and their characteristic values

	Symbol	Formula
Prandtl number	Pr	ν_l/α_l
Lewis number	Le	α_l/D_l
Darcy number	Da	K_0/L^2
Thermal Rayleigh number	Ra_T	$\beta_T\|\mathbf{g}\|(T_0-T_e)L^3/\nu_l\alpha_l$
Solutal Rayleigh number	Ra_C	$\beta_c\|\mathbf{g}\|(C_0-C_e)L^3/\nu_l\alpha_l$
Heat conductivity ratio	R_k	k_s/k_l
Heat capacity ratio	R_c	c_s/c_l

Table II. Governing equations for double-diffusive convection in a fluid-saturated porous medium.

$$\nabla\cdot\boldsymbol{v}(\boldsymbol{x},t)=0,\quad \boldsymbol{x}\in\Omega \tag{29}$$

$$\frac{\partial\boldsymbol{v}(\boldsymbol{x},t)}{\partial t} + \nabla\cdot\left(\frac{\boldsymbol{v}(\boldsymbol{x},t)\boldsymbol{v}(\boldsymbol{x},t)}{\epsilon(\boldsymbol{x},t)}\right) = -\nabla p(\boldsymbol{x},t)+\frac{p(\boldsymbol{x},t)}{\epsilon(\boldsymbol{x},t)}\nabla\epsilon(\boldsymbol{x},t)+\nabla\cdot[Pr(\,\nabla\boldsymbol{v}(\boldsymbol{x},t)+(\nabla\boldsymbol{v}(\boldsymbol{x},t))^T\,)] - \frac{(1-\epsilon(\boldsymbol{x},t))^2}{\epsilon^2(\boldsymbol{x},t)}\frac{Pr}{Da}\boldsymbol{v}(\boldsymbol{x},t)-\epsilon(\boldsymbol{x},t)\;Pr\;(Ra_T\;\theta(\boldsymbol{x},t)+Ra_C\;C_l(\boldsymbol{x},t))\;\boldsymbol{e_g},\quad \boldsymbol{x}\in\Omega \tag{30}$$

$$\frac{\partial h(\boldsymbol{x},t)}{\partial t}+\boldsymbol{v}(\boldsymbol{x},t)\cdot\nabla h_l(\boldsymbol{x},t)=\nabla\cdot[(\epsilon(\boldsymbol{x},t)+(1-\epsilon(\boldsymbol{x},t))R_k)\nabla\theta(\boldsymbol{x},t)],\quad \boldsymbol{x}\in\Omega \tag{31}$$

$$\frac{\partial C(\boldsymbol{x},t)}{\partial t}+\boldsymbol{v}(\boldsymbol{x},t)\cdot\nabla C_l(\boldsymbol{x},t)=\nabla\cdot\left(\frac{\epsilon(\boldsymbol{x},t)}{Le}\nabla C_l(\boldsymbol{x},t)\right),\quad \boldsymbol{x}\in\Omega \tag{32}$$

Initial conditions:

$$\boldsymbol{v}(\boldsymbol{x},0)=\mathbf{0},\quad h(\boldsymbol{x},0)=h_i,\quad C(\boldsymbol{x},0)=C_i,\quad \boldsymbol{x}\in\Omega \tag{33}$$

Boundary conditions:

$$\boldsymbol{v}(\boldsymbol{x},t)=\mathbf{0},\quad \boldsymbol{x}\in\Gamma \tag{34}$$

$$h(\boldsymbol{x},t)=h_s,\quad \boldsymbol{x}\in\Gamma^T \tag{35}$$

$$\frac{\partial h}{\partial n}(\boldsymbol{x},t)=0,\quad \boldsymbol{x}\in\Gamma^q \tag{36}$$

$$\frac{\partial C}{\partial n}(\boldsymbol{x},t)=0,\quad \boldsymbol{x}\in\Gamma \tag{37}$$

impermeable walls. For simplicity, a uniform initial temperature T_i and concentration C_i are assumed. Let us denote the region of interest by $\Omega \in \Re^{n_{sd}}$, where n_{sd} is the number of the space dimensions. The region Ω has a piecewise smooth boundary Γ which consists of Γ^T (boundary with prescribed temperature) and Γ^q (insulated boundary).

The non-dimensional governing equations are given in Table II where for simplicity we denote ϵ_l as ϵ, $< p_l >$ as p and the hat is dropped from the dimensionless variables. The pressure p used from now on refers to the volume-averaged dynamic pressure component. The vector $\boldsymbol{e_g}$ denotes the direction cosines of the gravity vector and for all two-dimensional examples reported later in this report the gravity acts vertically and downwards, i.e. $\boldsymbol{e_g} = [0.0,\ -1.0]^T$. Solution of the four coupled conservation equations will lead to the solution of the general thermal transport problem in porous media. The solution scheme to be presented in a later section treats this system of equations in an uncoupled fashion within each time step.

We will utilize the model of Table II to address convection in porous media as well as directional solidification of binary alloys. The additional conditions to those of Table II needed to account for a phase change process are reviewed next.

4. THERMODYNAMIC RELATIONS

In the above derived single-domain model, we have four governing equations but seven unknown variables: velocity $\boldsymbol{v}$, pressure p, mixture enthalpy h, mixture concentration C, temperature θ, liquid volume fraction ϵ, and liquid concentration C_l. To close the model, we need three supplementary relationships for θ, ϵ, and C_l.

By assuming that all phases in the averaging volume are in thermal equilibrium, that is, $\theta_l = \theta_s = \theta$, the general expression for the mixture enthalpy in terms of the temperature is:

$$h = (\epsilon + (1-\epsilon)R_c)\ \theta + \epsilon\ h_f + \frac{R_c T_e}{\Delta T} \tag{38}$$

where the last term in the equation comes from the non-dimensionalization process. Recall that T_e is used as the reference temperature in the definitions of dimensionless quantities given in Equation (28). Note that with these definitions, $\theta_e = 0$ and $C_e = 0$.

In this work, we consider a binary mixture with the phase diagram shown in Fig. 2 where the dimensionless slope of the liquidus line is denoted as $m < 0$ ($m = \frac{m_{\rm liq}\Delta C}{\Delta T}$). As discussed earlier, we assume that the liquid within the averaged volume is solutally well mixed, that is, $C_l = C_{\rm Liquidus}$. The local conservation of concentration can be expressed using the lever rule:

$$C = \epsilon\ C_l + (1-\epsilon)\ C_s \tag{39}$$

With the definition of the equilibrium partition ratio $k_p = C_s/C_l$, a direct relationship between the mixture concentration C and liquid concentration C_l is obtained.

The liquidus concentration and the temperature are related by:

$$C_{Liquidus} = \frac{\theta_m - \theta}{\theta_m} C_e \tag{40}$$

To simplify the presentation of update formulae for temperature θ, liquid concentration C_l

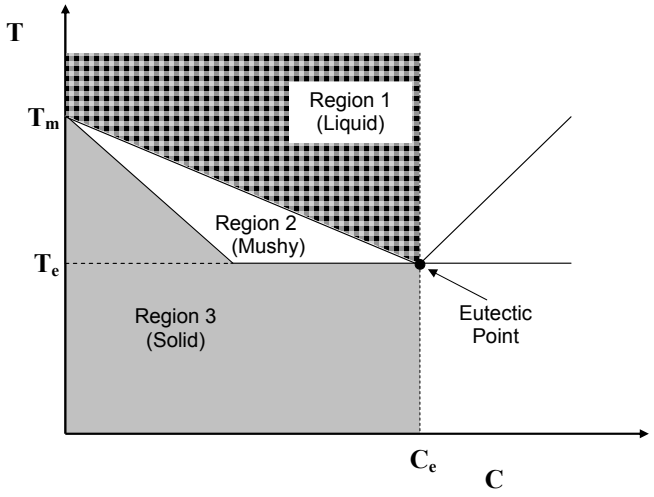

Figure 2. Typical equilibrium phase diagram for a binary alloy system. The regions shown here are used in the update formulae.

and liquid volume fraction ϵ, we first define some useful variables:

$$\theta_{\text{Liquidus}} = \theta_m + m(C + \frac{C_e}{\Delta C}) \tag{41}$$

$$\theta_{\text{Solidus}} = \max\{\theta_m + \frac{m}{k_p}(C + \frac{C_e}{\Delta C}),\, 0\} \tag{42}$$

$$h_{\text{Liquidus}} = \theta_{\text{Liquidus}} + R_c\frac{T_e}{\Delta T} + h_f \tag{43}$$

$$h_{\text{Solidus}} = R_c(\theta_{\text{Solidus}} + \frac{T_e}{\Delta T}) \tag{44}$$

$$h_e = R_c\frac{T_e}{\Delta T} + \left[1 - \frac{1}{1-k_p}\frac{\theta_{\text{Liquidus}}}{\theta_m}\right] h_f \tag{45}$$

With the definition of h_{Liquidus}, h_{Solidus} and h_e, the phase diagram is divided into three regions according to the relationships between the mixture enthalpy and the three critical enthalpy values:

- When $h > h_{\text{Liquidus}}$, the control volume is occupied by pure liquid, corresponding to region (1) in the phase diagram.
- When $h_e < h \leq h_{\text{Liquidus}}$, solidification has started but the liquid concentration has not reached the eutectic point, corresponding to region (2) in the phase diagram. In this region the volume fraction ϵ and temperature θ are solved iteratively using $\theta = \frac{h-\epsilon(\frac{T_e}{\Delta T}(R_c-1)+h_f)}{\epsilon+(1-\epsilon)R_c} - \frac{T_e}{\Delta T}$ and $\epsilon = [1 - \frac{1}{1-k_p}(\frac{\theta-\theta_{\text{Liquidus}}}{\theta-\theta_m})]$ subjected to the constraint $\theta_{\text{Solidus}} < \theta < \theta_{\text{Liquidus}}$. ϵ is also subjected to the constraint $\epsilon_e < \epsilon < 1.0$ to prevent oscillations, where ϵ_e is calculated as $\epsilon_e = [1 - \frac{1}{1-k_p}(\frac{\theta_{\text{Solidus}}-\theta_{\text{Liquidus}}}{\theta_{\text{Solidus}}-\theta_m})]$.

- When $h_{Solidus} < h \leq h_e$, the melt in the control volume is solidified at eutectic temperature and eutectic concentration.
- When $h \leq h_{\text{Solidus}}$, the alloy in the averaging volume is completely solidified, corresponding to region (3) in the phase diagram.

After calculating h_{Liquidus}, h_{Solidus} and h_e corresponding to a certain mixture concentration C, the following scheme is utilized to update the values of temperature, liquid concentration and liquid volume fraction:

- When $h > h_{\text{Liquidus}}$, $\theta = h - (R_c \frac{T_e}{\Delta T} + h_f)$, $\epsilon = 1$ and $C_l = C$.
- When $h_e < h \leq h_{Liquidus}$, θ and ϵ are calculated by iteratively solving $\theta = \frac{h - \epsilon(\frac{T_e}{\Delta T}(R_c - 1) + h_f)}{\epsilon + (1-\epsilon)R_c} - \frac{T_e}{\Delta T}$ and $\epsilon = [1 - \frac{1}{1-k_p}(\frac{\theta - \theta_{\text{Liquidus}}}{\theta - \theta_m})]$. Then, C_l is updated as follows: $C_l = \frac{C}{k_p + \epsilon(1-k_p)} + \frac{\frac{C_e}{\Delta C}(1-k_p)(1-\epsilon)}{k_p + \epsilon(1-k_p)}$.
- When $h_{\text{Solidus}} < h \leq h_e$, $\theta = 0$, $\epsilon = \frac{h - R_c \frac{T_e}{\Delta T}}{h_f}$ and $C_l = 0$.
- When $h \leq h_{\text{Solidus}}$, $\theta = \frac{h - \frac{T_e}{\Delta T} R_c}{R_c}$, $\epsilon = 0$ and $C_l = 0$.

5. A STABILIZED FINITE ELEMENT SCHEME FOR THE MOMENTUM EQUATIONS

Let us define the function spaces $S_{\boldsymbol{v}}$ and S_p as follows:

$$S_{\boldsymbol{v}} \stackrel{\text{def}}{=} \quad \{\boldsymbol{v} | \boldsymbol{v} \in (L_2(\Omega))^{\text{nsd}},\ \text{div}\boldsymbol{v} \ \in \ L_2(\Omega),\ \boldsymbol{v} = 0 \text{ on } \Gamma\} \tag{46}$$

$$S_p \stackrel{\text{def}}{=} \quad \{p | p \in L_2(\Omega),\ \int_\Omega p d\Omega = 0\} \tag{47}$$

The classical Galerkin formulation for the flow problem in Table II can be stated as follows: Find $\boldsymbol{V} \stackrel{\text{def}}{=} \{\boldsymbol{v}, p\} \in S_{\boldsymbol{v}} \times S_p$ such that for all $\boldsymbol{W} \stackrel{\text{def}}{=} \{\boldsymbol{w}, q\} \in S_{\boldsymbol{v}} \times S_p$ the following holds:

$$B(\boldsymbol{W}, \boldsymbol{V}) = L(\boldsymbol{W}) \tag{48}$$

where

$$\begin{aligned} B(\boldsymbol{W}, \boldsymbol{V}) &= \int_\Omega \boldsymbol{w} \cdot (\frac{\partial \boldsymbol{v}}{\partial t} + \boldsymbol{v} \cdot \nabla \left(\frac{\boldsymbol{v}}{\epsilon}\right) + \frac{(1-\epsilon)^2}{\epsilon^2} \frac{Pr}{Da} \boldsymbol{v}) d\Omega \ - \int_\Omega p \nabla \cdot \boldsymbol{w} d\Omega \\ &+ \int_\Omega Pr\ \nabla \boldsymbol{w} \cdot \left(\nabla \boldsymbol{v} \ + \ (\nabla \boldsymbol{v})^T\right) d\Omega + \int_\Omega q\ \nabla \cdot \boldsymbol{v} d\Omega \\ L(\boldsymbol{W}) &= \int_\Omega \frac{p}{\epsilon} \boldsymbol{w} \cdot \nabla \epsilon d\Omega - \int_\Omega \boldsymbol{w} \cdot \epsilon\ Pr(Ra_T \theta + Ra_C C_l) \boldsymbol{e_g} d\Omega \end{aligned} \tag{49}$$

The above formulation theoretically works only for certain velocity and pressure interpolations. In the finite element implementation of the Navier-Stokes equations, stabilizing techniques are needed to accommodate equal-order-interpolation velocity-pressure elements. The most common stabilization methods are the SUPG (Streamline-Upwind/Petrov-Galerkin) and the PSPG (Pressure-Stabilizing/Petrov-Galerkin) formulations proposed by many researchers (e.g. see Tezduyar et al. [23, 24]). These stabilizing terms can be obtained by many approaches including by minimizing the squared residual of the momentum equation,

i.e. following a least squares FEM approach [36]. As shown in [26], a proper stabilization term for pure Darcy flows is needed that differs in sign from that obtained by regular least squares approach.

In introducing the FEM used here, let us first define a modified pressure space S'_p as follows:

$$S'_p \stackrel{\text{def}}{=} \{p | p \in H^1(\Omega),\ \int_\Omega q d\Omega = 0\} \tag{50}$$

The stabilized weak form proposed here is the following: Find $\boldsymbol{V} = \{\boldsymbol{v}, p\} \in S_{\boldsymbol{v}} \times S'_p$ such that for all $\boldsymbol{W} = \{\boldsymbol{w}, q\} \in S_{\boldsymbol{v}} \times S'_p$ the following holds:

$$B_{\text{stab}}(\boldsymbol{W}, \boldsymbol{V}) = L_{\text{stab}}(\boldsymbol{W}) \tag{51}$$

where:

$$B_{\text{stab}}(\boldsymbol{W}, \boldsymbol{V}) = B(\boldsymbol{W}, \boldsymbol{V}) + \int_\Omega \mathcal{F}(\boldsymbol{v}, p) \cdot \mathcal{G}(\boldsymbol{w}, q) d\Omega + \int_\Omega \tau_5 \nabla \cdot \boldsymbol{v} \nabla \cdot \boldsymbol{w} d\Omega \tag{52}$$

$$L_{\text{stab}}(\boldsymbol{W}) = L(\boldsymbol{W}) + \int_\Omega \{\frac{p}{\epsilon} \nabla \epsilon - \epsilon\ Pr(Ra_T\ \theta + Ra_C\ C_l) \boldsymbol{e_g}\} \cdot \mathcal{G}(\boldsymbol{w}, q) d\Omega \tag{53}$$

where we defined:

$$\mathcal{F}(\boldsymbol{v}, p) = \frac{\partial \boldsymbol{v}}{\partial t} + \boldsymbol{v}_* \cdot \nabla \left(\frac{\boldsymbol{v}}{\epsilon}\right) + \nabla p + \frac{(1-\epsilon)^2}{\epsilon^2} \frac{Pr}{Da} \boldsymbol{v} - Pr \nabla^2 \boldsymbol{v} \tag{54}$$

$$\mathcal{G}(\boldsymbol{w}, q) = \tau_1 \boldsymbol{v}_* \cdot \nabla \left(\frac{\boldsymbol{w}}{\epsilon}\right) - \tau_2 \frac{(1-\epsilon)^2}{\epsilon^2} \frac{Pr}{Da} \boldsymbol{w} - \tau_3 Pr \nabla^2 \boldsymbol{w} + \tau_4 \nabla q \tag{55}$$

with $\boldsymbol{v}_*$ a divergence-free velocity that in the implementation of Equation (51) at a given time is usually taken as the known velocity at the previous time step.

The last term on the right hand side of Equation (52) is introduced to stabilize the incompressibility equation as discussed in [25]. The remaining stabilizing terms in Equations (52) and (53) can be derived by various techniques including a least squares procedure. However, note that the sign of the Darcy term used here is the reverse of that obtained by least squares [26]. This sign reversal first discussed in [26] was verified in our work as being essential for allowing the stabilized method to work even for the simplest problems of constant porosity. The particular values of the parameters $\tau_1, \ldots, \tau_5$ used in this work are introduced later in this section.

Let us now consider a given finite element partition $\bar{\Omega} = \bigcup_{e=1}^{n_{el}} \bar{\Omega}^e$. In this work, we assume that ϵ varies linearly within each element and is computed at the nodes as discussed in Section 4. To avoid high sensitivity of the fluid flow simulator on the variation of ϵ, a constant value of ϵ is taken for each element in the implementation of Equation (51). Thus the value of ϵ used in the flow simulator is evaluated at the centroid of each element. With this assumption, the terms in Equation (51) containing gradients of the porosity ϵ can be neglected. However, it is noted that a piece-wise linear variation of ϵ is maintained in the heat and mass transfer solvers.

We next define for the given finite element partition the spaces $S^h_{\boldsymbol{v}}$ and $S^{h'}_p$ as follows:

$$S^h_{\boldsymbol{v}} \stackrel{\text{def}}{=} \{\boldsymbol{v}^h | \boldsymbol{v}^h \in S_v,\ \boldsymbol{v}^h \in (C^o(\bar{\Omega}))^{n_{sd}},\ \boldsymbol{v}^h|_{\Omega^e} \in (P(\Omega^e))^{n_{sd}},\ e = 1, 2, \ldots, n_{el}\} \tag{56}$$

$$S^{h'}_p \stackrel{\text{def}}{=} \{p^h | p^h \in S_p,\ p^h \in C^o(\bar{\Omega}),\ p^h|_{\Omega^e} \in P(\Omega^e),\ e = 1, 2, \ldots, n_{el}\} \tag{57}$$

The final FEM is then posed as follows: Find $\boldsymbol{V}^h = \{\boldsymbol{v}^h, p^h\} \in S^h_{\boldsymbol{v}} \times S^{h'}_p$ such that for all $\boldsymbol{W}^h = \{\boldsymbol{w}^h, q^h\} \in S^h_{\boldsymbol{v}} \times S^{h'}_p$ the following holds:

$$B^h_{\text{stab}}(\boldsymbol{W}^h, \boldsymbol{V}^h) = L^h_{\text{stab}}(\boldsymbol{W}^h) \tag{58}$$

with

$$\begin{aligned} B^h_{\text{stab}}(\boldsymbol{W}^h, \boldsymbol{V}^h) = B^h(\boldsymbol{W}^h, \boldsymbol{V}^h) \quad &+ \quad \mathop{\mathsf{A}}_{e=1}^{n_{el}} \quad \int_{\Omega_e} \mathcal{F}^h(\boldsymbol{v}^h, p^h) \cdot \mathcal{G}^h(\boldsymbol{w}^h, q^h) d\Omega^e \\ &+ \quad \mathop{\mathsf{A}}_{e=1}^{n_{el}} \quad \int_{\Omega_e} \tau_5^e \nabla \cdot \boldsymbol{v}^h \nabla \cdot \boldsymbol{w}^h d\Omega^e \end{aligned} \tag{59}$$

$$L^h_{\text{stab}}(\boldsymbol{W}^h) = L^h(\boldsymbol{W}^h) \; + \quad \mathop{\mathsf{A}}_{e=1}^{n_{el}} \quad \int_{\Omega_e} -\epsilon \; Pr \; (Ra_T \; \theta^h + Ra_C \; C^h_l) \boldsymbol{e_g} \cdot \mathcal{G}^h(\boldsymbol{w}^h, q^h) d\Omega^e \tag{60}$$

where we have defined $\mathcal{F}^h(\boldsymbol{v}^h, p^h)$ and $\mathcal{G}^h(\boldsymbol{w}^h, q^h)$ as:

$$\mathcal{F}^h = \frac{\partial \boldsymbol{v}^h}{\partial t} + \boldsymbol{v}^h_* \cdot \nabla \left(\frac{\boldsymbol{v}^h}{\epsilon} \right) + \nabla p^h + \frac{(1-\epsilon)^2}{\epsilon^2} \frac{Pr}{Da} \boldsymbol{v}^h - Pr \nabla^2 \boldsymbol{v}^h \tag{61}$$

$$\mathcal{G}^h = \tau_1^e \boldsymbol{v}^h_* \cdot \nabla \left(\frac{\boldsymbol{w}^h}{\epsilon} \right) - \tau_2^e \frac{(1-\epsilon)^2}{\epsilon^2} \frac{Pr}{Da} \boldsymbol{w}^h - \tau_3^e Pr \nabla^2 \boldsymbol{w}^h + \tau_4^e \nabla q^h \tag{62}$$

$L^h(\boldsymbol{W}^h)$ is defined from Equation (49) by neglecting the contribution of the $\frac{p}{\epsilon}\nabla\epsilon$ term as discussed earlier.

The stabilizing contributions from the advective, Darcy, viscous and pressure terms are expressed as:

(A)	$\boldsymbol{\delta}^h = \frac{1}{\epsilon}\tau_1^e \boldsymbol{v}^h_* \cdot \nabla \boldsymbol{w}^h$	(advection term)
(B)	$\boldsymbol{\gamma}^h = -\tau_2^e \frac{(1-\epsilon)^2}{\epsilon^2} \frac{Pr}{Da} \boldsymbol{w}^h$	(Darcy term)
(C)	$\boldsymbol{\zeta}^h = -\tau_3^e \; Pr \nabla^2 \boldsymbol{w}^h$	(viscous term)
(D)	$\boldsymbol{\eta}^h = \tau_4^e \nabla q^h$	(pressure term)

It is easy to identify that the form of the stabilizing term $\boldsymbol{\delta}^h$ corresponds to the classical SUPG stabilizer and the form of $\boldsymbol{\eta}^h$ to the classical PSPG stabilizer, respectively. At the element interiors the contribution to the weighting function from the viscous term $\boldsymbol{\zeta}^h$ is identically zero for the P1P1 element and is neglected for the Q1Q1 element. The last stabilizing term, $\boldsymbol{\gamma}^h$, which we call DSPG, comes from the Darcy term and it is an important stabilizing term for the generalized Navier-Stokes/Darcy equations.

The stabilizing parameters for the advective and pressure terms are selected as follows:

$$\tau_1^e = \min_{\boldsymbol{x} \in \Omega^e} \left[\tau_{SUPG}, \; \frac{\epsilon^2(\boldsymbol{x})}{(1-\epsilon(\boldsymbol{x}))^2} \; \frac{Da}{Pr} \right] \qquad \text{for the convective term,} \tag{63}$$

$$\tau_4^e = \min_{\boldsymbol{x}\in\Omega^e}\left[\tau_{PSPG},\ \frac{\epsilon^2(\boldsymbol{x})}{(1-\epsilon(\boldsymbol{x}))^2}\ \frac{Da}{Pr}\right] \qquad \text{for the pressure term} \tag{64}$$

where τ_{SUPG}, τ_{PSPG} are defined as

$$\tau_{SUPG} = \frac{\epsilon h}{2\|\boldsymbol{v}^h\|} z(Re_{\boldsymbol{v}}) \tag{65}$$

$$\tau_{PSPG} = \frac{\epsilon h^{\#}}{2\|\boldsymbol{V}^h\|} z(Re_{\boldsymbol{V}}) \tag{66}$$

Here, $Re_{\boldsymbol{v}}$ and $Re_{\boldsymbol{V}}$ are the element Reynolds numbers, which are based on the local velocity $\boldsymbol{v}^h$ and a global scaling velocity $\boldsymbol{V}^h$ and are given by

$$Re_{\boldsymbol{v}} = \frac{\|\boldsymbol{v}^h\|h}{2Pr} \tag{67}$$

$$Re_{\boldsymbol{V}} = \frac{\|\boldsymbol{V}^h\|h^{\#}}{2Pr} \tag{68}$$

The element length h is computed by using the expression

$$h = 2\left(\sum_{e=1}^{n_{en}} |\mathbf{s}.\nabla N_\alpha^e|\right)^{-1} \tag{69}$$

where n_{en} is the number of nodes in the element, N_α^e is the basis function associated with the local node α, and $\mathbf{s}$ is the unit vector in the direction of the local velocity [23, 24, 25]. The element $h^{\#}$ on the other hand is defined to be the diameter of the circle which is area equivalent to the element. The function $z(Re)$ is defined as follows:

$$z(Re) = \begin{cases} Re/3 & 0 \le Re \le 3 \\ 1 & 3 \le Re \end{cases} \tag{70}$$

Stabilization forms similar to that in Equation (63) have been introduced earlier for the Stokes problem [37]-[39].

The stabilizing parameter τ_5^e is similar to τ_{LSIC} discussed in [25] and is given by

$$\tau_5^e = \frac{h}{2}\|\boldsymbol{v}^h\| \tag{71}$$

with h being defined in Equation (69). Slightly different forms for τ_5^e have been discussed in [25] and [40]. The present form holds good for convection dominated flows.

For the Darcy term, we select τ_2^e such that the stabilization takes the form $\boldsymbol{\gamma}^h = -(1-\epsilon)\boldsymbol{w}^h$, i.e.

$$\tau_2^e = \frac{\epsilon^2}{1-\epsilon}\frac{Da}{Pr} \tag{72}$$

Remark 1: The stabilization term γ^h induced by the Darcy flow varies linearly with ϵ transitioning from $\gamma^h = 0$ for a pure fluid phase ($\epsilon = 1$) to $\gamma^h = -\boldsymbol{w}^h$ towards a pure solid phase ($\epsilon \to 0$). Note also that for $\epsilon = 0$ (pure solid), the advection stabilization term $\boldsymbol{\delta}^h$

using Equation (63) becomes $\boldsymbol{\delta}^h = \lim_{\epsilon\to 0} \frac{1}{\epsilon}\left[\frac{\epsilon^2}{(1-\epsilon)^2}\ \frac{Da}{Pr}\right] = 0$. Thus the selection in Equation (63) allows for a stabilizing advection term that transitions from the classical SUPG values for a pure fluid to a zero contribution for a pure solid.

Remark 2: The stabilizing terms are linearized using quantities from the earlier time step or at the previous iteration at the current time step. For example, the advection stabilizing term at a particular time step is linearized using the velocity from the previous iteration denoted by $\boldsymbol{v}_*$. Same arguments apply for the stabilizing parameter τ_5^e defined in Equation (71). The Darcy stabilizing function, γ^h, is linearized using the liquid volume fraction, ϵ, known prior to the fluid flow solution at a particular time step. The stabilizing parameters τ_1^e and τ_4^e defined in Equations (63) and (64) are also linearized using the above mentioned procedures. Numerical simulations have shown that this linearization does not affect appreciably the convergence rate.

The spatial discretization of Equation (58) now leads to the following set of nonlinear ordinary differential equations:

$$[\mathbf{M}+\mathbf{M}_\delta+\mathbf{M}_\gamma]\{\dot{\boldsymbol{v}}\} + [\mathbf{N}(\boldsymbol{v})+\mathbf{N}_\delta(\boldsymbol{v})+\mathbf{N}_\gamma(\boldsymbol{v})]\{\boldsymbol{v}\} + [\mathbf{K}+\mathbf{K}_\delta+\mathbf{K}_\gamma]\{\boldsymbol{v}\}+\mathbf{C}_\Gamma\{\boldsymbol{v}\}$$
$$+[\mathbf{D}+\mathbf{D}_\delta+\mathbf{D}_\gamma]\{\boldsymbol{v}\} - [\mathbf{G}+\mathbf{G}_\delta+\mathbf{G}_\gamma]\{p\} = \{\mathbf{F}(\theta,C_l)+\mathbf{F}_\delta(\theta,C_l)+\mathbf{F}\gamma(\theta,C_l)\}, \tag{73}$$
$$\mathbf{M}_\eta\{\dot{\boldsymbol{v}}\} + \left(\mathbf{G}^T+\mathbf{N}_\eta(\boldsymbol{v})+\mathbf{K}_\eta+\mathbf{D}_\eta\right)\{\boldsymbol{v}\} + \mathbf{G}_\eta\{p\} = \{\mathbf{F}_\eta(\theta,C_l)\}, \tag{74}$$

where $\{\boldsymbol{v}\}$ is the vector of nodal values of $\boldsymbol{v}^h$, $\{\dot{\boldsymbol{v}}\}$ is the time derivative of $\{\boldsymbol{v}\}$, $\{p\}$ is the vector of nodal values of p^h. The matrices $\mathbf{M}$, $\mathbf{N}(\boldsymbol{v})$, $\mathbf{K}$, $\mathbf{D}$ and $\mathbf{G}$ are derived, respectively, from the time-dependent, advective, viscous, Darcy and pressure terms. Note that only explicit dependencies on primary solution variables are shown. The vector $\mathbf{F}$ is derived from the buoyancy term. The subscripts δ, η and γ identify the SUPG, PSPG and DSPG stabilizing terms, respectively. The subscript p is used here to denote the global velocity degrees of freedom in the final system of equations that corresponds to the i^{th} velocity degree of freedom of the elemental node α ($\alpha = 1,\ldots,n^e_{nodes}$) in the e^{th} element. Similarly, one can define q. We also introduce r and s to denote the global pressure degrees of freedom. We also denote the SUPG contribution as P^e_α, the PSPG contribution in the i^{th} $(i = 1,...,n_{sd})$ direction as $E^e_{\alpha i}$ and with D^e_α the DSPG contribution. They are defined as follows:

$$P^e_\alpha = \frac{1}{\epsilon}\tau^e_1 \boldsymbol{v}^h\cdot\nabla N^e_\alpha \tag{75}$$
$$E^e_{\alpha i} = \tau^e_4 N^e_{\alpha,i} \tag{76}$$
$$D^e_\alpha = -(1-\epsilon)N^e_\alpha \tag{77}$$

where ϵ in the above and following equations is referred to the constant value computed for the element e, i.e. $\epsilon = \epsilon(\boldsymbol{x}),\ \boldsymbol{x}\in\Omega^e$.

The various matrices forming the discrete finite element equations are described below.

$$[\mathbf{M}+\mathbf{M}_\delta+\mathbf{M}_\gamma]_{pq} = \mathop{\mathbf{A}}_{e=1}^{n_{el}} \int_{\Omega_e} (N^e_\alpha + P^e_\alpha + D^e_\alpha)N^e_\beta\delta_{ij}\ d\Omega^e \tag{78}$$

$$[\mathbf{N}(\boldsymbol{v})+\mathbf{N}_\delta(\boldsymbol{v})+\mathbf{N}_\gamma(\boldsymbol{v})]_{pq} = \mathop{\mathbf{A}}_{e=1}^{n_{el}} \int_{\Omega_e} \frac{1}{\epsilon}(N^e_\alpha + P^e_\alpha + D^e_\alpha)N^e_{\beta,k}v_k\ \delta_{ij}\ d\Omega^e \tag{79}$$

$$[\mathbf{K}+\mathbf{K}_\delta+\mathbf{K}_\gamma]_{pq} = \mathop{\mathbf{A}}_{e=1}^{n_{el}} \int_{\Omega_e} Pr(N^e_{\alpha,k}N^e_{\beta,k} - P^e_\alpha N^e_{\beta,kk} - D^e_\alpha N^e_{\beta,kk})\ \delta_{ij}\ d\Omega^e + \mathop{\mathbf{A}}_{e=1}^{n_{el}} \int_{\Omega_e} PrN^e_{\alpha,j}N^e_{\beta,i}\ d\Omega^e \tag{80}$$

$$[\mathbf{D}+\mathbf{D}_\delta+\mathbf{D}_\gamma]_{pq} = \mathop{\mathbf{A}}_{e=1}^{n_{el}} \int_{\Omega_e} \frac{(1-\epsilon)^2}{\epsilon^2}\frac{Pr}{Da}\ (N^e_\alpha + P^e_\alpha + D^e_\alpha)N^e_\beta\delta_{ij}\ d\Omega^e \tag{81}$$

$$[\mathbf{G}+\mathbf{G}_\delta+\mathbf{G}_\gamma]_{ps} = \mathop{\mathbf{A}}_{e=1}^{n_{el}} \int_{\Omega_e} (N^e_{\alpha,i}N^e_\beta - P^e_\alpha N^e_{\beta,i} - D^e_\alpha N^e_{\beta,i})\ d\Omega^e \tag{82}$$

$$[\mathbf{F}+\mathbf{F}_\delta+\mathbf{F}_\gamma]_p = \mathop{\mathbf{A}}_{e=1}^{n_{el}} \int_{\Omega_e} -\epsilon Pr\ (N^e_\alpha + P^e_\alpha + D^e_\alpha)(Ra_T\theta^e + Ra_C C^e_l)\boldsymbol{e_g}_i\ d\Omega^e \tag{83}$$

$$[\mathbf{C_\Gamma}]_{pq} = \mathop{\mathbf{A}}_{e=1}^{n_{el}} \int_{\Omega_e} \tau^e_5 N^e_{\alpha,i}N^e_{\beta,j}\ d\Omega \tag{84}$$

$$\left[\mathbf{G^T}\right]_{rq} = \mathop{\mathbf{A}}_{e=1}^{n_{el}} \int_{\Omega_e} N^e_\alpha\ N^e_{\beta,j}\ d\Omega^e \tag{85}$$

$$[\mathbf{M}_\eta]_{rq} = \mathop{\mathbf{A}}_{e=1}^{n_{el}} \int_{\Omega_e} E^e_{\alpha j}\ N^e_\beta\ d\Omega^e \tag{86}$$

$$[\mathbf{N}_\eta(\boldsymbol{v})]_{rq} = \mathop{\mathbf{A}}_{e=1}^{n_{el}} \int_{\Omega_e} \frac{1}{\epsilon}\ E^e_{\alpha j}\ v_k\ N^e_{\beta,k}\ d\Omega^e \tag{87}$$

$$[\mathbf{K}_\eta]_{rq} = \mathop{\mathbf{A}}_{e=1}^{n_{el}} \int_{\Omega_e} -PrE^e_{\alpha j}\ N^e_{\beta,kk}\ d\Omega^e \tag{88}$$

$$[\mathbf{D}_\eta]_{rq} = \mathop{\mathbf{A}}_{e=1}^{n_{el}} \int_{\Omega_e} \frac{(1-\epsilon)^2}{\epsilon^2}\ \frac{Pr}{Da}\ E^e_{\alpha j}\ N^e_\beta\ d\Omega^e \tag{89}$$

$$[\mathbf{G}_\eta]_{rs} = \mathop{\mathbf{A}}_{e=1}^{n_{el}} \int_{\Omega_e} E^e_{\alpha k}N^e_{\beta,k}\ d\Omega^e \tag{90}$$

$$[\mathbf{F}_\eta]_r = \mathop{\mathbf{A}}_{e=1}^{n_{el}} \int_{\Omega_e} -\epsilon E^e_{\alpha k}Pr\ \boldsymbol{e_g}_k(Ra_T\theta^e + Ra_C C^e_l)\ d\Omega^e \tag{91}$$

where δ_{ij} stands for the Kronecker delta. The time integration of the Equations (73, 74) is performed using a backward Euler scheme, i.e.

$$\dot{\boldsymbol{v}} = \frac{\boldsymbol{v}^n - \boldsymbol{v}^{n-1}}{\Delta t} \tag{92}$$

The resulting nonlinear algebraic equations are solved by the Newton-Raphson method as discussed next.

Remark 3: Various other forms of stabilization parameters were considered. Let $\mathcal{R}_{\boldsymbol{v}}$ denote the residual of the momentum equation. Following the approach of [40], we consider the

evaluation of τ when various terms dominate in their residual. For each case, one can approximate $\tau = \left(\frac{\partial \mathcal{R}\boldsymbol{v}}{\partial \boldsymbol{v}}\right)^{-1}$. For example, when advection dominates, one can show that $\tau_{conv} \approx \frac{\epsilon h}{2\|\boldsymbol{v}^h_{n-1}\|}$, here $h/2$ is the representative elemental length given by the distance between the centroid of an element and its boundary [40]. Similarly one can compute $\tau_{diff} \approx \frac{h^2}{4Pr}$ and $\tau_{Darcy} \approx \frac{Da}{Pr}\left(\frac{\epsilon}{1-\epsilon}\right)^2$ in the diffusive and Darcy flow regimes, respectively. Following [25], [40] and others, one can then approximate a unified value for τ applicable to all regimes:

$$\tau_{stab} = \left(\frac{1}{\tau_{conv}^{n_{sd}}} + \frac{1}{\tau_{diff}^{n_{sd}}} + \frac{1}{\tau_{Darcy}^{n_{sd}}}\right)^{-1/n_{sd}} \tag{93}$$

For transient problems, an extra contribution of a τ in the form $\Delta t/2$ is introduced in the expression for τ_{stab} above as suggested in [23] and [25]. Variations of this forms were also considered including using a global scaling velocity $\boldsymbol{V}^h$ instead of the local elemental velocity $\boldsymbol{v}^h$ in the computation of τ in the pressure stabilizing function $\boldsymbol{\eta}^h$. These forms of stabilization parameter did not result yet in stable simulations in particular in the implementation of high Ra number melt flow in solidification processes. More research in this direction is currently in progress.

Remark 4: Using the approach highlighted in Remark 3, τ_2^e results in a Darcy stabilization term of the form $\boldsymbol{\gamma}^h = -\boldsymbol{w}^h$. Even though this term is appropriate for pure Darcy flows (see [26]), it did not lead to stable solutions for flows in media with varying porosity ϵ. Considering that the contribution of the Darcy stabilizing term should vanish as ϵ increases towards a pure fluid phase ($\epsilon = 1$), we herein select τ_2^e such that $\boldsymbol{\gamma}^h = -(1-\epsilon)\boldsymbol{w}^h$.

Remark 5: The subgrid scale or multiscale approach introduced in [41] can also be applied to the generalized Navier-Stokes/Darcy equations. The formulation involves a subgrid scale decomposition of the exact solution $(\boldsymbol{v}, p)$ into a numerical finite element approximation $(\boldsymbol{v}^h, p^h)$ and an unresolvable or subgrid part $(\boldsymbol{v}', p')$. The formulation obtained from the subgrid scale model is of the same form as the present model given by Equation (58) (including the sign and form of the Darcy stabilizing term). The difference lies in the selection of the stabilizing parameters τ. In the subgrid scale method τ can assume a unified form as e.g. given in Equation (93), which incorporates the advective, Darcy and diffusive effects in a single parameter. As discussed in Remark 3, more work is needed in selecting a unified stabilizing parameter τ appropriate for all regimes of ϵ ($0 \leq \epsilon \leq 1$).

5.1. Solution Strategy

Let us denote $\hat{\mathbf{M}} = \mathbf{M} + \mathbf{M}_\delta + \mathbf{M}_\gamma$. Similar notation is introduced for $\hat{\mathbf{N}}$, $\hat{\mathbf{K}}$, $\hat{\mathbf{D}}$, $\hat{\mathbf{G}}$ and $\hat{\mathbf{F}}$. Therefore, the resulting nonlinear algebraic equations are written as:

$$\begin{aligned} g_1(\boldsymbol{v}_n, p_n) &= \hat{\mathbf{M}}\,(\boldsymbol{v}_n - \boldsymbol{v}_{n-1}) + (\hat{\mathbf{N}}(\boldsymbol{v}_n) + \hat{\mathbf{K}} + \hat{\mathbf{D}} + \mathbf{C}_{\boldsymbol{\Gamma}})\Delta t \boldsymbol{v}_n - \hat{\mathbf{G}}\Delta t p_n \\ &- \hat{\mathbf{F}}(\mathbf{T}, \mathbf{C})\Delta t = 0 \end{aligned} \tag{94}$$

$$\begin{aligned} g_2(\boldsymbol{v}_n, p_n) &= \mathbf{M}_\eta\,(\boldsymbol{v}_n - \boldsymbol{v}_{n-1}) + (\mathbf{G}^{\mathbf{T}} + \mathbf{N}_\eta(\boldsymbol{v}_n) + \mathbf{K}_\eta + \mathbf{D}_\eta)\Delta t \boldsymbol{v}_n \\ &+ \mathbf{G}_\eta \Delta t p_n - \mathbf{F}_\eta(\mathbf{T}, \mathbf{C})\Delta t = 0 \end{aligned} \tag{95}$$

This set of nonlinear equations is solved using the Newton-Raphson method. Suppose $(\boldsymbol{v}_n^{i-1}, p_n^{i-1})$ is known, the algorithm to compute $(\boldsymbol{v}_n^{i}, p_n^{i})$ is as follows (with i here an iteration index):

1. Form the residual $\mathbf{R}$ evaluated at $(\boldsymbol{v}_n^{i-1}, p_n^{i-1})$:

$$\begin{aligned} R_1 = g_1 &= [\hat{\mathbf{M}}\boldsymbol{v}_n^{i-1} + \left(\hat{\mathbf{N}}(\boldsymbol{v}_n^{i-1}) + \hat{\mathbf{K}} + \hat{\mathbf{D}} + \mathbf{C}_{\mathbf{\Gamma}}\right)\Delta t\boldsymbol{v}_n^{i-1} \\ &- \hat{\mathbf{G}}\Delta t p_n^{i-1}] - \hat{\mathbf{F}}\Delta t - \hat{\mathbf{M}}\boldsymbol{v}_{n-1} \end{aligned} \tag{96}$$

$$\begin{aligned} R_2 = g_2 &= [\mathbf{M}_\eta \boldsymbol{v}_n^{i-1} + \left(\mathbf{N}_\eta(\boldsymbol{v}_n^{i-1}) + \mathbf{G}^{\mathbf{T}} + \mathbf{K}_\eta + \mathbf{D}_\eta\right)\Delta t\boldsymbol{v}_n^{i-1} \\ &+ \mathbf{G}_\eta \Delta t p_n^{i-1}] - \mathbf{F}_\eta \Delta t - \mathbf{M}_\eta \boldsymbol{v}_{n-1} \end{aligned} \tag{97}$$

2. Compute the Jacobian matrix $\mathbf{J}$ evaluated at $(\boldsymbol{v}_n^{i-1}, p_n^{i-1})$:

$$\begin{aligned} J_{11} &= \frac{\partial g_1}{\partial \boldsymbol{v}_n} = \hat{\mathbf{M}} + \frac{\partial \hat{\mathbf{N}}}{\partial \boldsymbol{v}}\Delta t\boldsymbol{v}_n^{i-1} + (\hat{\mathbf{N}} + \hat{\mathbf{K}} + \hat{\mathbf{D}} + \mathbf{C}_{\mathbf{\Gamma}})\Delta t \\ J_{12} &= \frac{\partial g_1}{\partial p_n} = -\hat{\mathbf{G}}\Delta t \\ J_{21} &= \frac{\partial g_2}{\partial \boldsymbol{v}_n} = \mathbf{M}_\eta + \frac{\partial \mathbf{N}_\eta}{\partial \boldsymbol{v}}\Delta t\boldsymbol{v}_n^{i-1} + (\mathbf{N}_\eta + \mathbf{G}^{\mathbf{T}} + \mathbf{K}_\eta + \mathbf{D}_\eta)\Delta t \\ J_{22} &= \frac{\partial g_2}{\partial p_n} = \mathbf{G}_\eta \Delta t \end{aligned} \tag{98}$$

3. Solve the linearized equations:

$$J \cdot \left\{ \begin{array}{c} dv^i \\ dp^i \end{array} \right\} = \left\{ \begin{array}{c} -R_1 \\ -R_2 \end{array} \right\} \tag{99}$$

   The preconditioned bi-conjugate gradient iterative solver (BiCGStab) is used to solve this system of equations for most of the time steps. LU-factorization was performed only at a few time steps in the beginning of the transient solution process.
4. Do a full Newton step and update $\boldsymbol{v}$ and p: $\boldsymbol{v}_n^{i+1} = \boldsymbol{v}_n^i + d\boldsymbol{v}^i$ and $p_n^{i+1} = p_n^i + dp^i$.

To avoid singularity of J in Equation (99), the minimum value of ϵ allowed in the simulation is taken as $\epsilon_{num} = 1 \times 10^{-3}$. This value of ϵ is used here to identify the solid phase.

6. NUMERICAL SCHEME FOR THE ENERGY AND SPECIES EQUATION

A classical SUPG formulation is used for the solution of the energy and species conservation equations. The energy and species equations are first cast into the standard form of a convection-diffusion scalar equation. We first consider the energy equation. In dimensional form the enthalpy h can be expressed as:

$$h = \epsilon h_l + (1-\epsilon)h_s, \qquad h_s = c_s T, \qquad h_l = c_l T + h_l^0 \tag{100}$$

Here h_l^0 is the reference enthalpy and is expressed as $(c_s - c_l)T_e + h_f$, with h_f being the latent heat of melting at the eutectic temperature T_e (here taken as the reference temperature). The following equation then holds:

$$h_l - h = (1-\epsilon)[(c_l - c_s)(T - T_e) + h_f] \tag{101}$$

In the non-dimensional form, we can write:

$$\hat{h}_l = \hat{h} + (1-\epsilon)[(1-R_c)\theta + \hat{h}_f] \tag{102}$$

Following our earlier convention, for convenience we drop the hat from dimensionless fields.

Referring to [42], one can approximate $\nabla\theta$ as follows:

$$\nabla\theta^n \approx \alpha^{n-1}\nabla h^n \tag{103}$$

with n denoting the time step and α^n defined element-wise as:

$$\alpha^n = \begin{cases} \frac{\nabla\theta^n(\boldsymbol{x})\cdot\nabla h^n(\boldsymbol{x})}{|\nabla h^n(\boldsymbol{x})|^2} & \text{if } |\nabla h^n(\boldsymbol{x})| > 0, \\ \\ \frac{d\theta}{dh}(\boldsymbol{x}) & \text{if } |\nabla h^n(\boldsymbol{x})| = 0, \end{cases}$$

Using Equation (102) and the above approximation, Equation (31) is written as:

$$\begin{aligned} \frac{\partial h(\boldsymbol{x},t)}{\partial t} + \boldsymbol{v}(\boldsymbol{x},t)\cdot\nabla h(\boldsymbol{x},t) &= -\boldsymbol{v}(\boldsymbol{x},t)\cdot\nabla[(1-\epsilon)((1-R_c)\theta(\boldsymbol{x},t)+h_f)] \\ &\quad +\nabla\cdot[(\epsilon + (1-\epsilon)R_k)\alpha\nabla h(\boldsymbol{x},t)] \end{aligned} \tag{104}$$

We also define the following finite element interpolation function space for h^h:

$$S^h_\theta = \{h^h \mid h^h \in C^o(\bar{\Omega}),\ h^h|_{\Omega^e} \in P^l(\Omega^e),\ e = 1,2,\ldots,n_{el}, h^h \doteq 0 \ \text{ on } \Gamma\} \tag{105}$$

The weak formulation of Equation (104) can be stated as follows: Find $h^h \in S^h_\theta$ such that, $\forall\ \hat{w}^h \in S^h_\theta$:

$$\begin{aligned} \int_\Omega \hat{w}^h \left(\frac{\partial h^h}{\partial t} + \boldsymbol{v}^h\cdot\nabla h^h\right) d\Omega + \int_\Omega \nabla\hat{w}^h\cdot\left((\epsilon+(1-\epsilon)R_k)\alpha\nabla h^h\right) d\Omega \\ + \mathop{\mathsf{A}}_{e=1}^{n_{el}} \int_{\Omega^e} \hat{\delta}^h \left(\frac{\partial h^h}{\partial t} + \boldsymbol{v}^h\cdot\nabla h^h\right) d\Omega^e \\ = -\int_\Omega \hat{w}^h \left(\boldsymbol{v}^h\cdot\nabla[(1-\epsilon)((1-R_c)\theta^h + h^h_f)]\right) d\Omega \\ - \mathop{\mathsf{A}}_{e=1}^{n_{el}} \int_{\Omega^e} \hat{\delta}^h \left(\boldsymbol{v}^h\cdot\nabla[(1-\epsilon)((1-R_c)\theta^h + h^h_f)]\right) d\Omega^e \end{aligned} \tag{106}$$

The spatial discretization of Equation (106) leads to the following ordinary differential equation:

$$[\hat{\mathbf{M}} + \hat{\mathbf{M}}_\delta]\{\dot{h}\} + [\hat{\mathbf{N}} + \hat{\mathbf{N}}_\delta]\{h\} + [\hat{\mathbf{K}} + \hat{\mathbf{K}}_\delta]\{h\} = \{\hat{\mathbf{F}} + \hat{\mathbf{F}}_\delta\} \tag{107}$$

The element stiffness matrices and the load vector are given as follows:

$$\left[\hat{\mathbf{M}} + \hat{\mathbf{M}}_\delta\right]_{pq} = \mathop{\mathsf{A}}_{e=1}^{n_{el}} \int_{\Omega_e} (N^e_\alpha + \delta^e_\alpha) N^e_\beta d\Omega^e \tag{108}$$

$$\left[\hat{\mathbf{N}}(\boldsymbol{v}) + \hat{\mathbf{N}}_\delta(\boldsymbol{v})\right]_{pq} = \mathop{\mathsf{A}}_{e=1}^{n_{el}} \int_{\Omega_e} (N^e_\alpha + \delta^e_\alpha) v^e_k N^e_{\beta,k} d\Omega^e \tag{109}$$

$$\left[\hat{\mathbf{K}}+\hat{\mathbf{K}}_\delta\right]_{pq} = \mathop{\mathbf{A}}_{e=1}^{n_{el}} \int_{\Omega_e} (\epsilon+(1-\epsilon)R_k)\ \alpha\ N^e_{\alpha,k}N^e_{\beta,k}d\Omega^e \tag{110}$$

$$\left[\hat{\mathbf{F}}+\hat{\mathbf{F}}_\delta\right]_{pq} = \mathop{\mathbf{A}}_{e=1}^{n_{el}} \int_{\Omega_e} -(N^e_\alpha+\delta^e_\alpha)[(1-\epsilon)(1-R_c)\ \theta^h_{,k}\ v^h_k - v^h_k\epsilon_{,k}((1-R_c)\theta^h+h_f)]d\Omega^e \tag{111}$$

Using a similar argument, we rewrite Equation (32) as:

$$\begin{aligned}\frac{\partial C(\boldsymbol{x},t)}{\partial t}+\boldsymbol{v}(\boldsymbol{x},t)\cdot\nabla C(\boldsymbol{x},t) &= \nabla\cdot\Big(\frac{\epsilon}{Le}\nabla C(\boldsymbol{x},t)\Big)\\ +\boldsymbol{v}(\boldsymbol{x},t)\cdot\nabla(C(\boldsymbol{x},t) &- C_l(\boldsymbol{x},t))+\nabla\cdot\Big(\frac{\epsilon}{Le}\nabla(C_l(\boldsymbol{x},t)-C(\boldsymbol{x},t))\Big)\end{aligned} \tag{112}$$

Recasting the species equation in this form allows accounting for the effect of the liquid concentration C_l via a body force term and in addition allows for an easy implementation of different microscopic diffusion models.

The weak formulation of Equation (112) can be stated as follows: Find $C^h \in S^h_C$ such that, $\forall\ \tilde{w}^h \in S^h_C$:

$$\begin{aligned}&\int_\Omega \tilde{w}^h\left(\frac{\partial C^h}{\partial t}+\boldsymbol{v}^h\cdot\nabla C^h\right)d\Omega+\int_\Omega\nabla\tilde{w}^h\cdot(\frac{\epsilon}{Le}\nabla C^h)d\Omega\\ &\quad+\mathop{\mathbf{A}}_{e=1}^{n_{el}}\int_{\Omega^e}\tilde{\delta}^h\left(\frac{\partial C^h}{\partial t}+\boldsymbol{v}^h\cdot\nabla C^h\right)d\Omega^e\\ &=\int_\Omega\tilde{w}^h[(\boldsymbol{v}^h\cdot\nabla(C^h-C^h_l))+\nabla\cdot\Big(\frac{\epsilon}{Le}\nabla(C^h_l-C^h)\Big)]d\Omega\\ +\mathop{\mathbf{A}}_{e=1}^{n_{el}}&\int_{\Omega^e}\tilde{\delta}^h[(\boldsymbol{v}^h\cdot\nabla(C^h-C^h_l))+\nabla\cdot\Big(\frac{\epsilon}{Le}\nabla(C^h_l-C^h)\Big)]d\Omega^e\end{aligned} \tag{113}$$

This weak form can be modified as follows:

$$\begin{aligned}&\int_\Omega \tilde{w}^h\left(\frac{\partial C^h}{\partial t}+\boldsymbol{v}^h\cdot\nabla C^h_l\right)d\Omega+\int_\Omega\nabla\tilde{w}^h\cdot(\frac{\epsilon}{Le}\nabla C^h)d\Omega\\ &\quad+\mathop{\mathbf{A}}_{e=1}^{n_{el}}\int_{\Omega^e}\tilde{\delta}^h\left(\frac{\partial C^h}{\partial t}+\boldsymbol{v}^h\cdot\nabla C^h_l\right)d\Omega^e\\ &=\int_\Omega\tilde{w}^h[\nabla\cdot\Big(\frac{\epsilon}{Le}\nabla(C^h_l-C^h)\Big)]d\Omega\\ +\mathop{\mathbf{A}}_{e=1}^{n_{el}}&\int_{\Omega^e}\tilde{\delta}^h[\nabla\cdot\Big(\frac{\epsilon}{Le}\nabla(C^h_l-C^h)\Big)]d\Omega^e\end{aligned} \tag{114}$$

The spatial discretization of Equation (114) leads to the following ordinary differential equation:

$$[\tilde{\mathbf{M}}+\tilde{\mathbf{M}}_\delta]\{\dot{C}\}+[\tilde{\mathbf{N}}+\tilde{\mathbf{N}}_\delta]\{C_l\}+[\tilde{\mathbf{K}}+\tilde{\mathbf{K}}_\delta]\{C\}=\{\tilde{\mathbf{F}}+\tilde{\mathbf{F}}_\delta\} \tag{115}$$

The element stiffness matrices and the load vector are given as follows:

$$\left[\tilde{\mathbf{M}}+\tilde{\mathbf{M}}_\delta\right]_{pq} = \mathop{\mathbf{A}}_{e=1}^{n_{el}} \int_{\Omega^e} (N^e_\alpha+\delta^e_\alpha)N^e_\beta d\Omega^e \tag{116}$$

$$\left[\tilde{\mathbf{N}}(\boldsymbol{v})+\tilde{\mathbf{N}}_{\delta}(\boldsymbol{v})\right]_{pq} = \mathop{\mathbf{A}}_{e=1}^{n_{el}} \int_{\Omega^e} (N^e_\alpha + \delta^e_\alpha) v^e_k N^e_{\beta,k} d\Omega^e \tag{117}$$

$$\left[\tilde{\mathbf{K}}+\tilde{\mathbf{K}}_{\delta}\right]_{pq} = \mathop{\mathbf{A}}_{e=1}^{n_{el}} \int_{\Omega^e} \frac{\epsilon}{Le} N^e_{\alpha,k} N^e_{\beta,k} d\Omega^e \tag{118}$$

$$\left[\tilde{\mathbf{F}}+\tilde{\mathbf{F}}_{\delta}\right]_{pq} = \mathop{\mathbf{A}}_{e=1}^{n_{el}} \int_{\Omega^e} (N^e_\alpha + \delta^e_\alpha) \left[\frac{\epsilon}{Le} \left(C_{l,kk} - C_{,kk}\right)\right] d\Omega^e \tag{119}$$

Let us denote:

$$\hat{\mathbf{M}} = [\tilde{\mathbf{M}} + \tilde{\mathbf{M}}_{\delta}] \tag{120}$$

with similar notation being used for $\hat{\mathbf{N}}$, $\hat{\mathbf{K}}$, and $\hat{\mathbf{F}}$. The resulting non-linear equations for enthalpy and solute concentration can be expressed as:

$$\hat{\mathbf{M}}\left(\frac{h_n - h_{n-1}}{\Delta t}\right) + (\hat{\mathbf{N}}(\boldsymbol{v}_n) + \hat{\mathbf{K}}) h_n = \hat{\mathbf{F}}_{\mathbf{T}} \tag{121}$$

$$\hat{\mathbf{M}}\left(\frac{C_n - C_{n-1}}{\Delta t}\right) + \hat{\mathbf{N}}(\boldsymbol{v}_n) C_{l_n} + \hat{\mathbf{K}} C_n = \hat{\mathbf{F}}_{\mathbf{C}} \tag{122}$$

These equations are solved by the multistep predictor corrector method. The convection term is linearized using the velocity $\boldsymbol{v}_{n-1}$ from the previous time step. Let us denote as $\dot{h}$ the enthalpy rate. With known h_n and $\dot{h}_n$, the algorithm below computes h_{n+1} and $\dot{h}_{n+1}$:

1. Predictor step ($0.5 \leq \gamma \leq 1$):

$$h^{(0)}_{n+1} = h_n + \Delta t(1-\gamma)\dot{h}_n \tag{123}$$

$$\dot{h}^{(0)}_{n+1} = 0 \tag{124}$$

2. Solve $\mathbf{M}^* \Delta \dot{h}^i_{n+1} = \mathbf{R}^i_{n+1}$, where

$$\mathbf{M}^* = \hat{\mathbf{M}} + \gamma \Delta t (\hat{\mathbf{K}} + \hat{\mathbf{N}}) \qquad \text{and} \tag{125}$$

$$\mathbf{R}^i_{n+1} = \mathop{\mathbf{A}}_{e=1}^{n_{el}} \left(\hat{f}^e - \hat{m}^e \dot{h}^{e(i)}_{n+1} - (\hat{n}^e(\boldsymbol{v}_{n-1}) + \hat{k}^e) h^{e(i)}_{n+1}\right) \tag{126}$$

   with $\hat{f}^e$, $\hat{m}^e$, $\hat{n}^e(\boldsymbol{u}_{n-1})$ and $\hat{k}^e$ representing the respective vectors and matrices at the element level.
3. Corrector step:

$$h^{(i)}_{n+1} = h^i_{n+1} + \Delta t \gamma \Delta \dot{h}^i_{n+1} \tag{127}$$

$$\dot{h}^{(i)}_{n+1} = \dot{h}^{(i)}_{n+1} + \Delta \dot{h}^i_{n+1} \tag{128}$$

4. Repeat steps 2 and 3 until convergence in h_{n+1} is achieved.

The solution strategy for C_{n+1} (solute solver) is similar to that used for h_{n+1}. The matrix $\mathbf{M}^*$ used is $\hat{\mathbf{M}} + \gamma \Delta t \hat{\mathbf{K}}$ but in the fluid phase (when $C = C_l$), $\mathbf{M}^*$ is modified as $\mathbf{M}^* = \hat{\mathbf{M}} + \gamma \Delta t (\hat{\mathbf{N}}(\boldsymbol{v}_{n-1}) + \hat{\mathbf{K}})$.

7. COUPLING OF THE VARIOUS SUBPROBLEMS AND OVERALL TIME INTEGRATION SCHEME

The various subproblems considered here include the thermal, flow, solute species problems as well as the update formulae for example the thermodynamical relations describing the phase transformation, enthalpy/temperature relation, etc. The tolerance level used to define convergence in all three main solution steps (heat, solute and momentum) is set at 10^{-12}. The error criterion is based on the relative error in the solutions obtained between Newton-Raphson iterations within a time step. For example, in the fluid flow solver, the error norm is defined as $\|\Delta U^{i+1}\|/\|U_n^{i+1}\|$ where $U = [\boldsymbol{v}, p]$. The overall algorithm is summarized below:

1. At time t_n, all fields such as velocity $\boldsymbol{v}_n$, enthalpy h_n, temperature θ_n, concentration C_n, liquid volume fraction ϵ_n, etc. are known.
2. Advance to time step $t_{n+1} = t_n + \Delta t$. Set j=0, $\boldsymbol{v}_{n+1}^{j=0} = \boldsymbol{v}_n$, $h_{n+1}^{j=0} = h_n$, $\epsilon_{n+1}^{j=0} = \epsilon_n$, etc., where j is an iteration index and the subscript denotes the time level.
3. Compute the mixture enthalpy h_{n+1}^{j+1} using the algorithm described in Section 6 (Equations (123)-(128)).
4. Compute the mixture concentration C_{n+1}^{j+1} using the algorithm described in Section 6.
5. Update the temperature θ_{n+1}^{j+1}, liquid concentration ${C_l}_{n+1}^{j+1}$ and liquid volume fraction ϵ_{n+1}^{j+1} using the scheme described in Section 4.
6. Repeat steps 3 to 5 so that $\|\theta_{n+1}^{j+1} - \theta_{n+1}^{j}\| < \epsilon_{tol}$, $\|{C_l}_{n+1}^{j+1} - {C_l}_{n+1}^{j}\| < \epsilon_{tol}$, $\|\epsilon_{n+1}^{j+1} - \epsilon_{n+1}^{j}\| < \epsilon_{tol}$ are all satisfied ($\epsilon_{tol} = 10^{-8}$ here denotes appropriate tolerance). If convergence is satisfied, set $h_{n+1} = h_{n+1}^{j+1}$, $C_{n+1} = C_{n+1}^{j+1}$ and $\epsilon_{n+1} = \epsilon_{n+1}^{j+1}$.
7. Compute the mixture velocity $\boldsymbol{v}_{n+1}^{j+1}$ and pressure $p_{l_{n+1}}^{j+1}$ using the algorithm of Section 5.1. Upon convergence, set $\boldsymbol{v}_{n+1} = \boldsymbol{v}_{n+1}^{j+1}$, $n = n + 1$ and proceed to step 2.

8. NUMERICAL EXAMPLES

To test the applicability of the macroscopic transport equations to the solid/liquid two-phase system, a series of fluid flow problems in porous media are investigated using the present model. All the example problems for flow in porous media have been taken from Nithiarasu et al. [21, 22]. We then proceed to model a directional binary alloy solidification example.

8.1. Example 1: Double diffusive convection in a constant porosity medium

We consider a square cavity filled with a liquid of constant porosity. The main equations to be solved are the momentum, energy and solute equations. A quadratic drag force term is included in addition to the Darcy term in order to allow us to compare the present method with the results given in [21]. The non-dimensional form of the momentum equation with the quadratic drag force is as follows:

$$\frac{\partial \boldsymbol{v}}{\partial t} + \boldsymbol{v} \cdot \nabla \left(\frac{\boldsymbol{v}}{\epsilon}\right) = -\frac{Pr}{Da}\frac{(1-\epsilon)^2}{\epsilon^2}\boldsymbol{v} - \frac{1.75\|\boldsymbol{v}\|(1-\epsilon)}{(150\,Da)^{1/2}\epsilon^2}\boldsymbol{v} + Pr\nabla^2\boldsymbol{v} - \epsilon\nabla p - \epsilon Pr[Ra_T\theta + Ra_c C]\mathbf{e}_g$$

The energy equation is now expressed in terms of the temperature and the species equation is similar to that discussed in the beginning of this report with the liquid concentration C_l

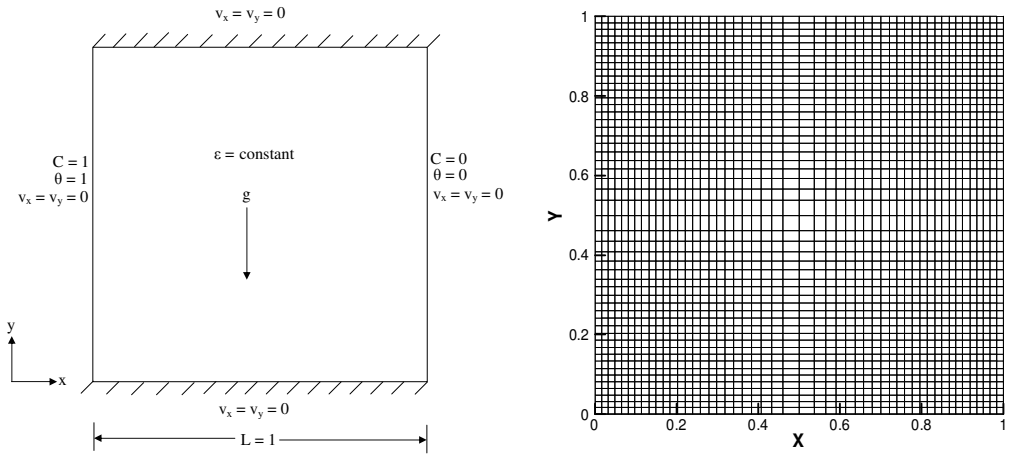

Figure 3. Flow in a constant porosity medium: $Ra_T = 2 \times 10^8$, $Ra_c = -1.8 \times 10^8$, $Da = 7.407 \times 10^{-7}$, $Pr = 1.0$, $\epsilon = 0.6$, $Le = 2.0$. A finite element mesh of 50×50 bilinear elements is used (Example 1).

replaced by concentration C. These are given by

$$\frac{\partial \theta}{\partial t} + \boldsymbol{v} \cdot \nabla \theta = \nabla^2 \theta \tag{129}$$

$$\epsilon \frac{\partial C}{\partial t} + \boldsymbol{v} \cdot \nabla C = \nabla . \left(\frac{\epsilon}{Le} \nabla C \right) \tag{130}$$

The non-dimensional variables used here are defined as in Equation (28) with $\Delta T = T_w - T_i$, $\Delta C = C_w - C_i$ and $T_e = T_i$. The subscripts w and i refer to the wall and initial conditions, respectively, and $R_k = R_c = 1$.

The boundary and initial conditions for this problem are as follows:

- at $x = 0$: $v_x = v_y = 0$, $\theta = 1$, $C = 1$
- at $x = 1$: $v_x = v_y = 0$, $\theta = 0$, $C = 0$
- at $y = 0$: $v_x = v_y = 0$, $\partial\theta/\partial n = 0$, $\partial C/\partial n = 0$
- at $y = 1$: $v_x = v_y = 0$, $\partial\theta/\partial n = 0$, $\partial C/\partial n = 0$

The problem domain along with the boundary conditions and the finite element mesh consisting of 50×50 bilinear Q4 elements is shown in Figure 3. The steady-state solution consisting of the non-dimensional temperature and concentration fields and the stream function are shown in Figure 4. These results compare very well with those reported in [21]. The time step size used was varied starting from 0.00002 at early times to 0.0005 towards steady-state. Note that the isotherms and iso-concentration lines were significantly affected by convection in the porous region. With this example, double diffusive convection in a constant porosity medium was simulated successfully thereby laying the foundations for solving more complex problems in the following examples.

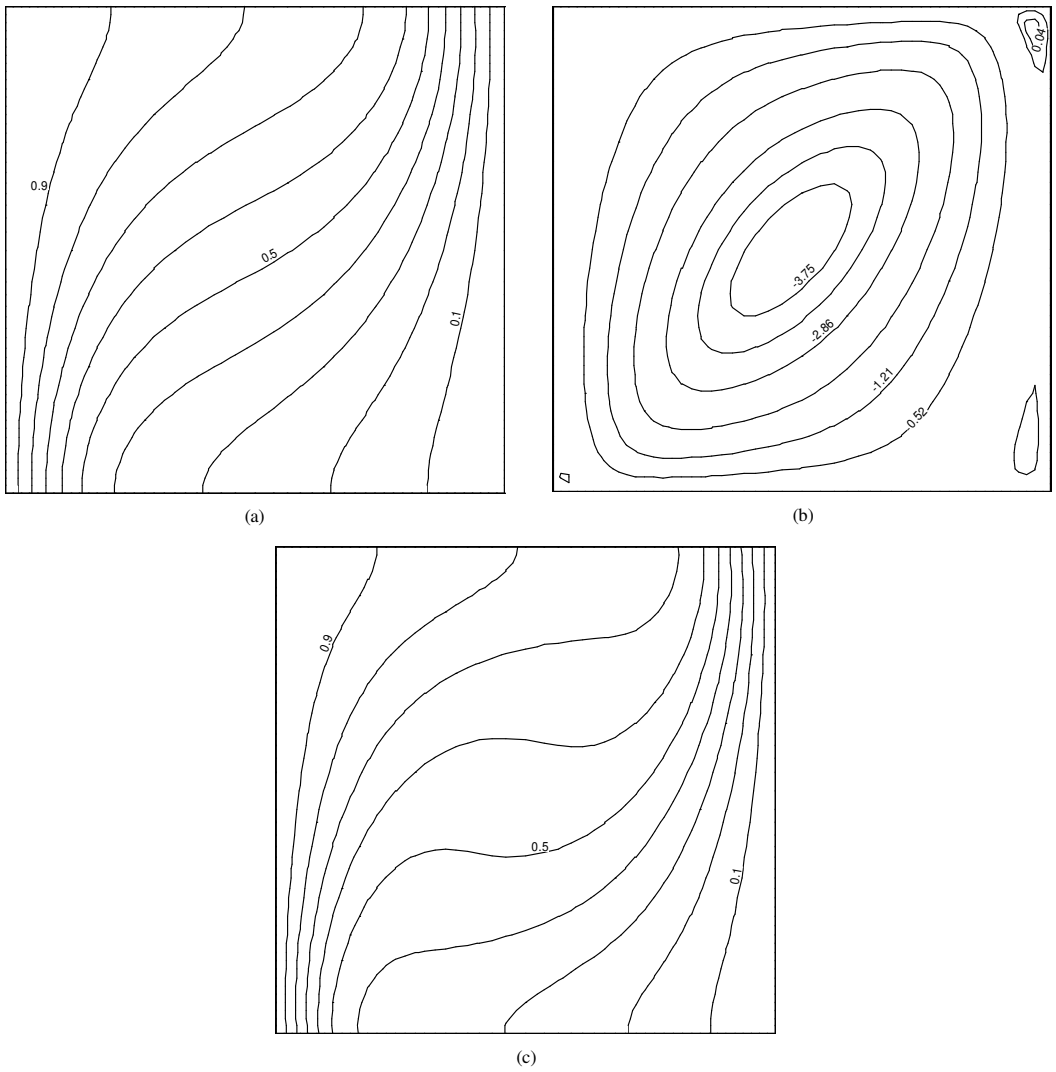

Figure 4. Isotherms, stream function contours and iso-concentration lines for flow in a constant porosity medium (Example 1).

8.2. Example 2: Natural convection in a fluid saturated variable porosity medium

The second example considers natural convection in a variable porosity medium. This problem is obtained from [22]. The dimensionless 1×1 domain along with the boundary conditions for velocity and temperature are shown in Figure 5. The dimensionless length ℓ is taken as $\ell = 0.3$. The equations involved here are the same as those of Example 1 except that there is no species equation. The wall porosity ϵ_w is taken as 0.4. The porosity increases linearly from 0.4 at the wall to 1.0 (pure liquid) at the core. We considered two grids for the solution of this problem,

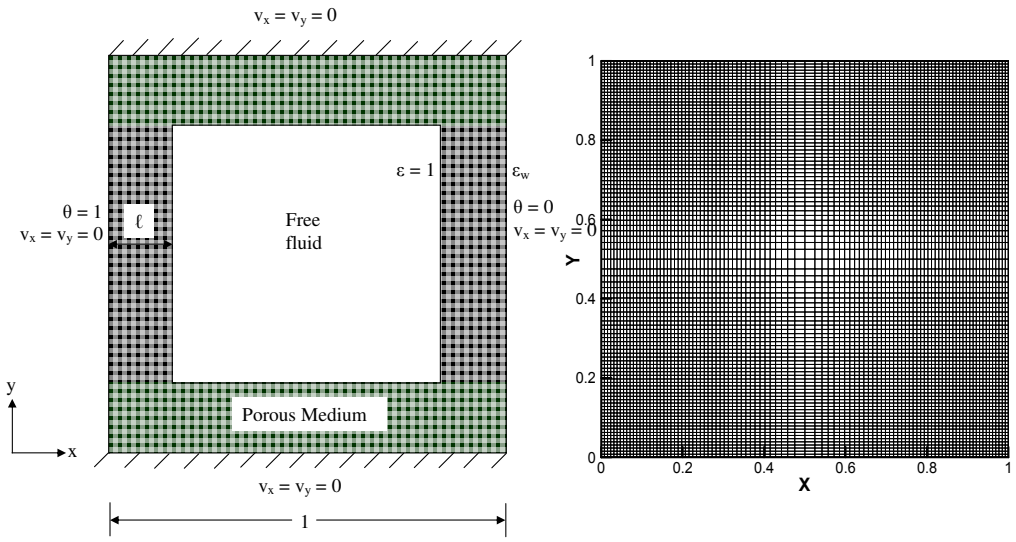

Figure 5. Geometry and boundary conditions for the cavity filled with a variable porosity medium. The finite element mesh consisting of 100×100 bilinear elements is also shown here (Example 2).

50×50 and 100×100, both slightly biased finite element meshes of bilinear Q4 elements. For the coarse grid case, the time step size was varied from 0.00005 to 0.0005 and for the finer grid case between 0.00005 to 0.0001. The finer finite element mesh is shown in Figure 5. The steady state solutions obtained from the two grids are nearly identical indicating convergence of the algorithm. The solution obtained with the finer grid is shown in Figure 6. Note that the obtained results are close but do not match fully with those of [22] where no convergence studies were conducted. It is also noted that in our own implementation of the method of [22] using SUPG stabilization of the predictor and corrector flow solvers, the fractional step algorithm could not converge when using the tied tolerance limits (10^{-12}) set in this example. In the current stabilized FEM implementation, a quadratic convergence was observed in the flow solver and the algorithm was successfully completed in two to three iterations in each time step. The present example problem was repeated for the case with $\ell = 0.2$ and using an 80×80 mesh. The results are shown in Figure 7. From the computed isotherms, it is evident that convection was dominant in the liquid core. In the porous region towards the boundaries with decreasing porosity, conduction was still dominant.

8.3. Example 3: Binary alloy solidification with advection

This example considers the solidification of an aqueous mixture of ammonium chloride and water ($NH_4Cl - H_2O$). This semi-transparent alloy system has been selected in many studies mainly because it permits flow visualization [43]. Important physical constants and the non-dimensional parameters used here are summarized in Tables III and IV, respectively. The domain consists of a rectangular cavity of size 25 mm $\times$ 100 mm. Initially, all boundaries are insulated, the cavity is charged with a superheated binary solution consisting of 70% water

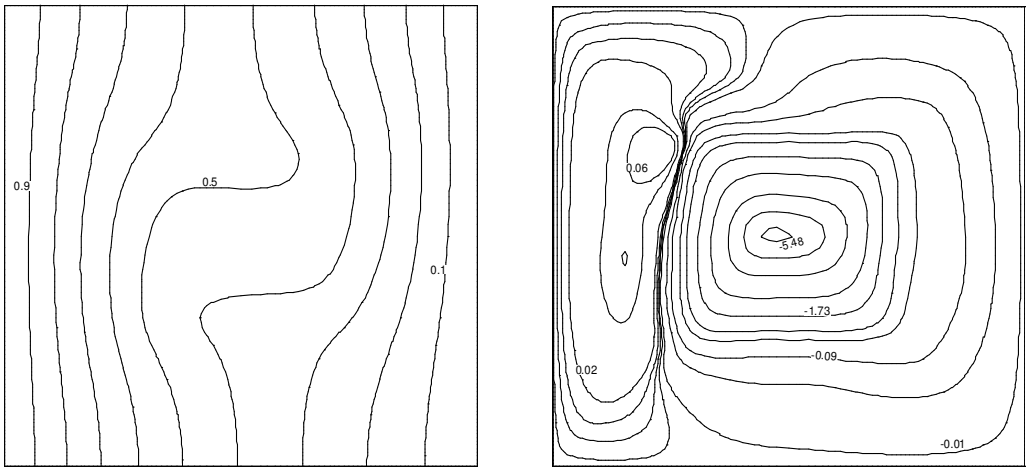

Figure 6. Isotherms and stream function with a 100×100 mesh (see Fig. 5) for natural convection in a fluid saturated variable porosity medium for the case $Ra_T = 1 \times 10^6$, $Pr = 1.0$, $Da = 6.665 \times 10^{-7}$, $\epsilon_w = 0.4$ and $\ell = 0.3$. (Example 2).

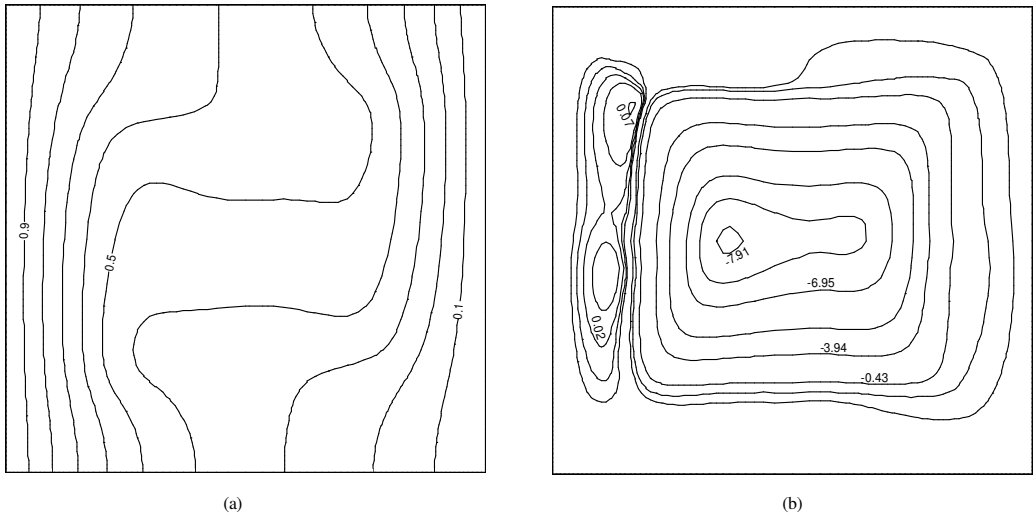

Figure 7. Isotherms and stream function for natural convection in a fluid saturated variable porosity medium for the case $Ra_T = 1 \times 10^6$, $Pr = 1.0$, $Da = 6.665 \times 10^{-7}$, $\epsilon_w = 0.4$, $\ell = 0.2$ and an 80×80 grid (Example 2).

and 30% ammonium chloride and temperature 311 K and the system is in equilibrium. At time $t = 0^+$, the temperature of the left vertical wall is suddenly reduced to and maintained at 223 K, which is less than the eutectic temperature 257.75 K. The right vertical wall is maintained at the initial temperature, whereas the top and bottom horizonal walls remain insulated.

In the implementation of this example, various bounds were applied in the update formulae of Section 4. These bounds include preventing the enthalpy h from taking values higher than $h_{\max}$ (the enthalpy of the hot wall, here 5.5997) or smaller than $h_{\min}$ (the enthalpy of the cold wall, here 2.41). Similarly, the upper values of ϵ and C_l were set to 1. In the fluid flow solver, θ and C_l are both bounded by the expression min(calculated value, 1.0) to prevent spurious oscillations.

A 50×50 mesh consisting of 2500 bilinear ($Q4$) elements and 2601 nodes was taken for this example. The results obtained at the non-dimensional times $t = 0.009, 0.018, 0.036, 0.071$ and 0.142 are shown in Figures 8-12, respectively. The time step used for this example was varied from 0.00001 at early times to 0.00002 near the end.

A comparison between the maximum velocity $|v_{max}|$ and stream function ψ calculated here with those reported in [7] is given in Tables V and VI, respectively. While the overall nature and magnitude of these results are similar, some quantitative differences exist. This discrepancy may be due to a large extent to the slightly different form of the governing equations used in [7] where the convective term did not have an ϵ in the denominator, which as shown here arises from the volume averaging process. In addition, the buoyancy terms were characterized by a missing ϵ term and the form of the Darcy drag term was $Pr(1-\epsilon)^2/Da\ \epsilon^3$ which arises directly from the Kozeny-Karman relationship. In the governing equations discussed here, the Darcy drag term takes the form $Pr(1-\epsilon)^2/Da\ \epsilon^2$ which represents final volume-averaged form. The equations here are similar to those discussed in [15] where the governing equations are derived from volume-averaging. However, no results or numerical implementation were presented in [15].

As can be seen from Figures 8-12, convection in the melt was thermally driven by heating from the hot right wall and cooling through the solid and mushy zones. Solutally driven flow was predicted in the mushy zone. The thermal and solutal buoyancy forces are opposing each other due to the fact that water, the lighter solute of the two, was rejected into the liquid. The two coupled flow mechanisms induced significant deviation from conduction dominated conditions, and the thickness of the fully solidified and mushy regions varied with vertical position. Furthermore, as a result of variations in thermal and solutal conditions near the liquidus interface separating the mushy and melted zones, the shape of the liquidus interface was highly irregular. The streamlines in these figures reveal more clearly the thermally driven (counterclockwise) cell in the melt and the solutal driven (clockwise) cell in the mushy zone. It is clear that the temperature and liquid composition fields have been distorted significantly by advection effects.

The evolution of macrosegregation patterns was particularly studied. The steady-state mixture concentration plot is shown in Figure 13. In Figures 10-12, there is a region where the liquidus penetrates into the mushy zone. Within this region, interdendritic fluid is channeled. The subsequent effects are revealed by the mixture concentration plot of Figure 13.

Table III. Physical constants for the 30% NH_4Cl - 70% H_2O system

	Symbol	Value
Density of the solid	$\rho_s(kgm^{-3})$	1078
Density of the liquid	$\rho_l(kgm^{-3})$	1078
Thermal conductivity of the solid	$k_s(Wm^{-1}K^{-1})$	0.393
Thermal conductivity of the liquid	$k_l(Wm^{-1}K^{-1})$	0.468
Solid specific heat	$c_s(Jkg^{-1}K^{-1})$	1870
Liquid specific heat	$c_l(Jkg^{-1}K^{-1})$	3249
Diffusion coefficient	$D(m^2/s)$	4.8×10^{-9}
Viscosity of the liquid	$\mu(kgm^{-1}s^{-1})$	1.3×10^{-3}
Latent heat	$h_f(Jkg^{-1})$	3.138×10^5
Permeability coefficient	$K_0(m^2)$	5.56×10^{-11}
Thermal expansion coefficient	$\beta_T(K^{-1})$	3.832×10^{-4}
Solutal expansion coefficient	β_c	0.257
Eutectic temperature	$T_e(K)$	257.75
Eutectic composition	C_e	0.803
$NH_4Cl - H_2O$ melting point	$T_m(K)$	633.59
Equilibrium partition ratio	k_p	0.30

Table IV. Dimensionless groups and their characteristic values

	Symbol	Value
Prandtl number	Pr	9.025
Lewis number	Le	27.84
Darcy number	Da	8.896×10^{-8}
Thermal Rayleigh number	Ra_T	1.938×10^7
Solutal Rayleigh number	Ra_c	-2.514×10^7
Dimensionless slope of the liquidus	m	0.905
Heat conductivity ratio	R_k	0.840
Heat capacity ratio	R_c	0.576

Table V. A comparison between maximum velocities calculated here and those reported in [7]

Non-dimensional time	$\lvert u_{max}\rvert_{calculated}(mm/s)$	$\lvert u_{max}\rvert_{reported}(mm/s)$
0.009	6.94	5.5
0.018	6.62	7.4
0.036	7.03	8.1
0.071	7.38	7.8
0.142	7.26	7.9

Table VI. A comparison between stream function in the pure liquid and porous region calculated here, and those reported in [7]

	$\psi_{calculated}$		$\psi_{reported}$	
Non-dimensional time	$\psi_{max,l}$	$\lvert\psi_{max,s+l}\rvert$	$\psi_{max,l}$	$\lvert\psi_{max,s+l}\rvert$
0.009	1.71×10^{-2}	7.38×10^{-4}	1.53×10^{-2}	6.05×10^{-4}
0.018	1.32×10^{-2}	9.08×10^{-4}	1.70×10^{-2}	8.26×10^{-4}
0.036	1.47×10^{-2}	7.78×10^{-4}	2.04×10^{-2}	6.74×10^{-4}
0.071	1.78×10^{-2}	4.45×10^{-4}	1.71×10^{-2}	1.97×10^{-4}
0.142	1.81×10^{-2}	1.41×10^{-4}	1.71×10^{-2}	6.19×10^{-5}

9. CONCLUSIONS

A stabilized FEM formulation and implementation was presented for coupled transport processes in porous media and for modeling melt flow in binary alloy solidification processes. The governing macroscopic transport equations were derived by volume-averaging the microscopic equations. Through various numerical examples it was concluded that the present model converges nearly quadratically. Other methods implemented by the authors (including the fractional step method) did not show such rates of convergence and in many occasions failed to converge to the tolerance levels set in the examples presented here. More research is currently conducted using the subgrid multiscale phenomena approach in order to compute a unified stabilizing parameter τ that works well for all regions of porosity.

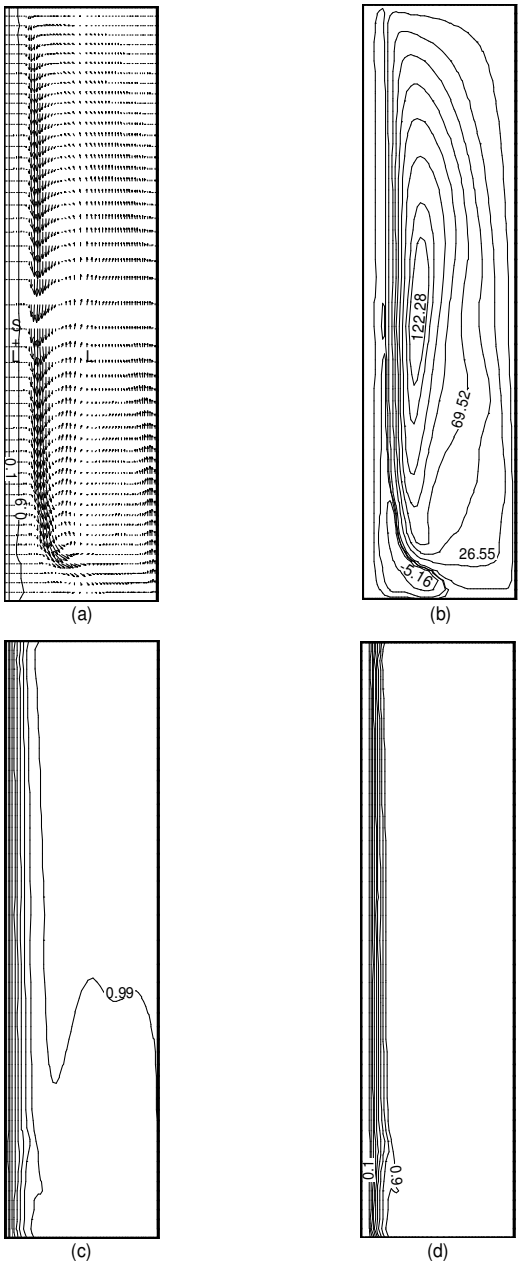

Figure 8. Solidification behavior at t = 0.009: (a) velocity vectors (v_{max} = 6.94 mm/s), (b) streamlines, (c) isotherms, (d) liquid concentration lines (Example 3).

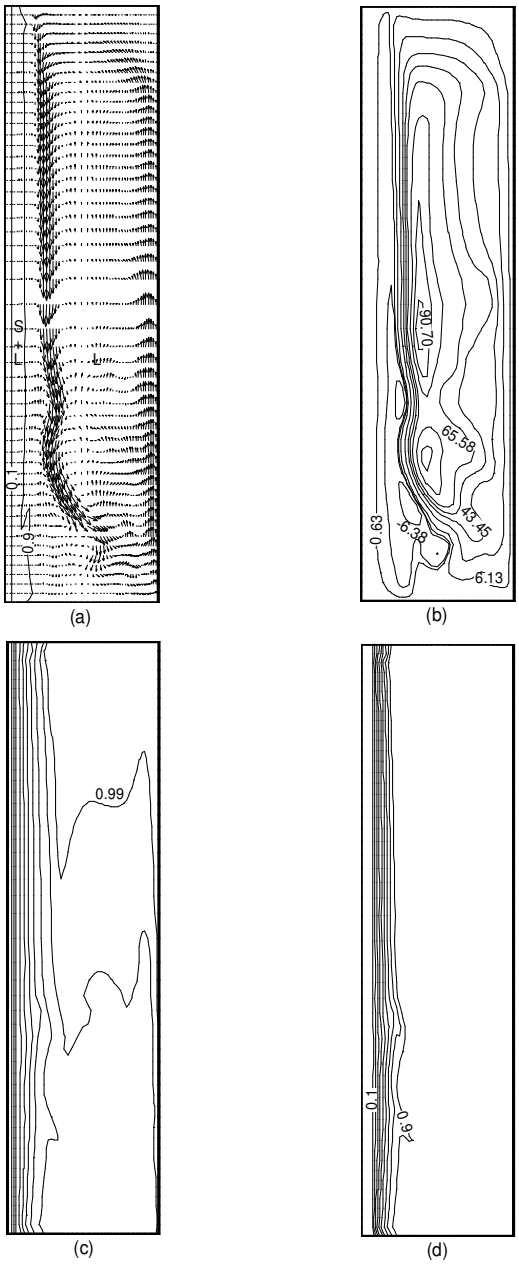

Figure 9. Solidification behavior at $t = 0.018$: (a) velocity vectors ($v_{max} = 6.62$ mm/s), (b) streamlines, (c) isotherms and (d) liquid concentration lines (Example 3).

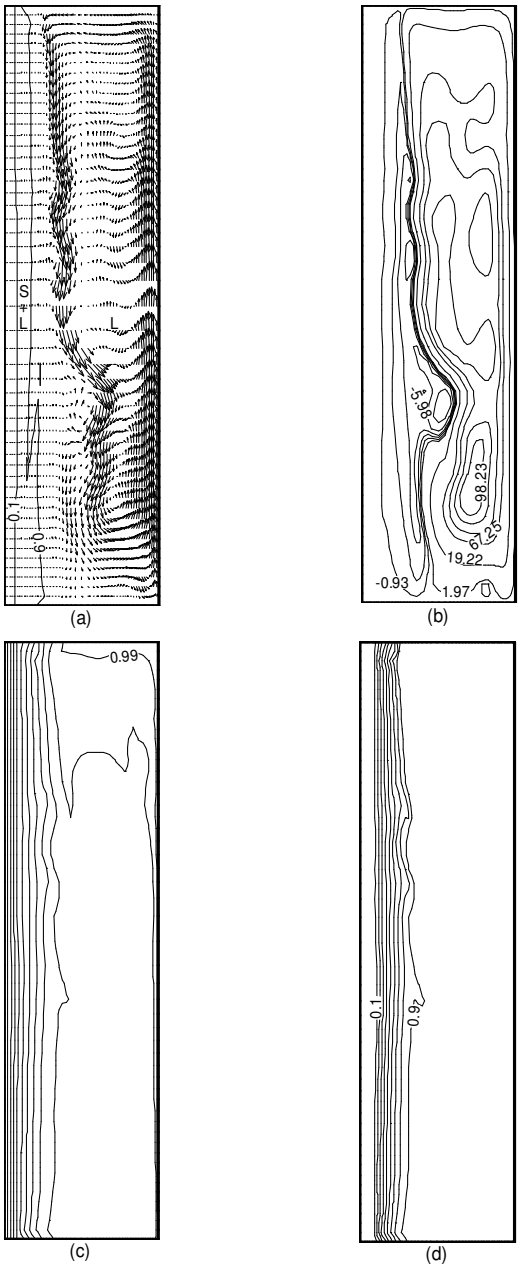

Figure 10. Solidification behaviour at t = 0.036: (a) velocity vectors (v_{max} = 7.03 mm/s), (b) streamlines, (c) isotherms and (d) liquid concentration lines (Example 3).

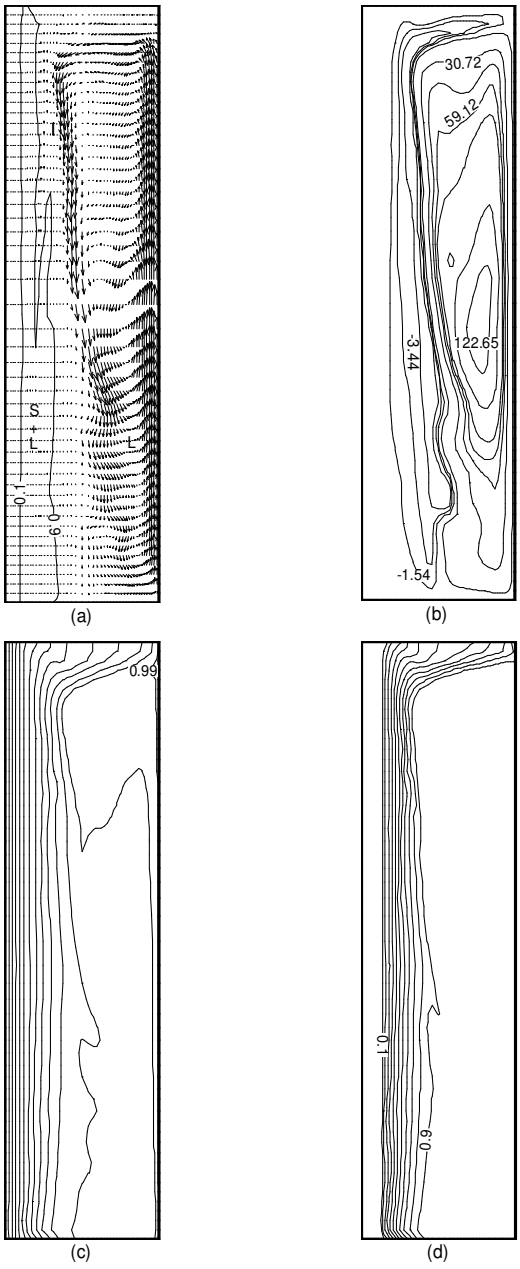

Figure 11. Solidification behavior at t = 0.071: (a) velocity vectors (v_{max} = 7.38 mm/s) (b) streamlines,(c) isotherms and (d) liquid concentration lines (Example 3).

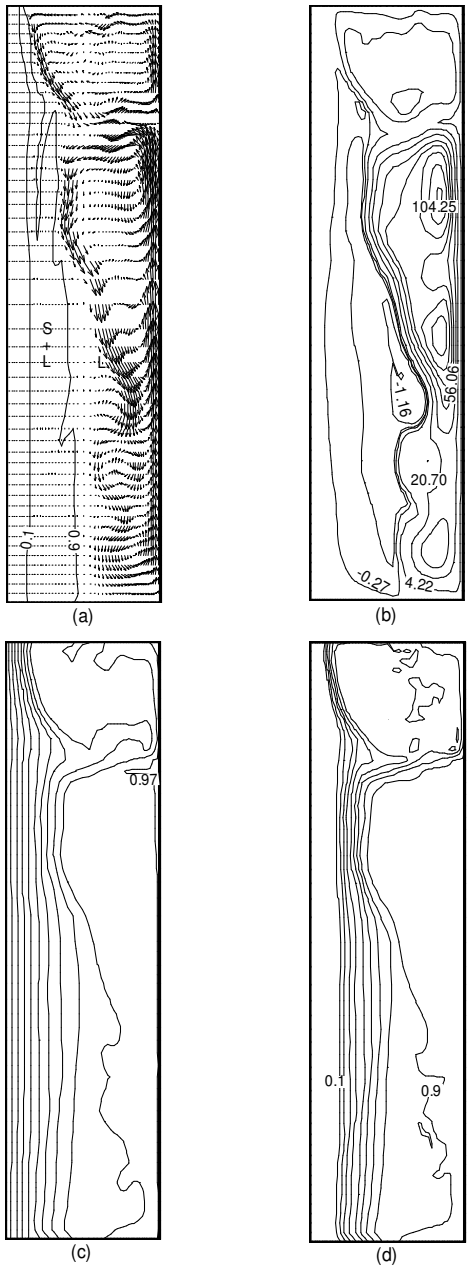

Figure 12. Solidification behavior at $t = 0.142$: (a) velocity vectors ($v_{max} = 7.26$ mm/s), (b) streamlines, (c) isotherms and (d) liquid concentration lines (Example 3).

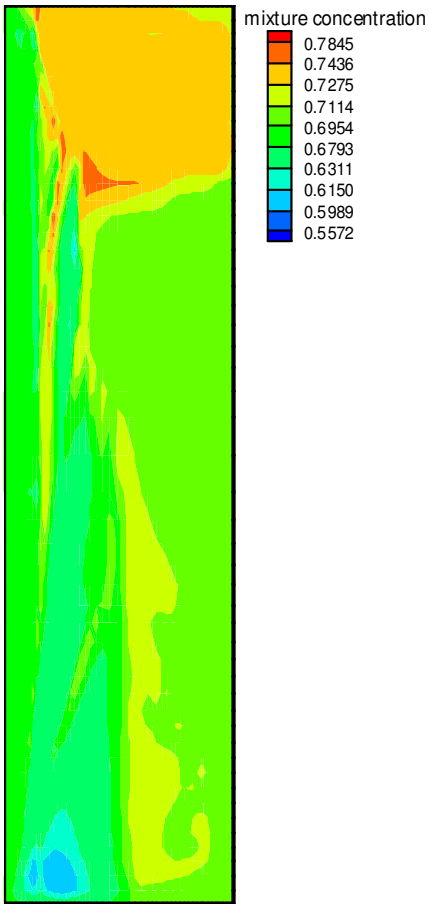

Figure 13. Macrosegregation patterns at $t = 0.142$ (Example 3).

10. ACKNOWLEDGEMENTS

The work presented here was funded in part by the NASA Physical Sciences Division, Materials Science Program (98-HEDS-05) and by the University-Industry Partnerships for Aluminum Industry of the Future Program of the Office of Industrial Technologies of the U.S. Department of Energy (DE-FC07-02ID14396) with additional matching support from Alcoa. This research was conducted using the resources of the Cornell Theory Center. The authors will also like to thank Prof. A. Masud for introducing them to his work in [26] with Prof. T. J. R. Hughes. The contributions of Mrs. Lei Wan in the early stages of this work are appreciated. Mr. Lijian Tan from our laboratory developed parallel implementations of the methods discussed here and independently validated the presented results. The authors will finally like to thank the three

anonymous reviewers for their comments that helped us to significantly improve the revised manuscript.

REFERENCES

1. Kurz W, Fisher DJ. *Fundamentals of Solidification* (3nd edn). Trans. Tech. Publications: SA, Switzerland, 1989.
2. Shyy W, Udaykumar HS, Rao MM, Smith RW. *Computational Fluid Dynamics with Moving Boundaries* (1st edn). Tailor and Francis: Washington, D.C., 1996.
3. Sampath R, Zabaras N. An object oriented implementation of a front tracking finite element method for directional solidification processes. *International Journal for Numerical Methods in Engineering* 1999; **44**: 1227-1265.
4. Prantil VC, Dawson PR. Application of mixture theory to continuous casting. *Am. Soc. Mech. Eng.* 1983; **29**: 47-54.
5. Hills RN, Loper DE, Roberts PH. A Mathematically consistent model of a mushy zone. *Q. J. Mech. Appl. Math* 1983; **36**: 505-539.
6. Incropera FP, Bennon WD. A continuum model for momentum, heat and species transport in binary solid-liquid phase change systems - I. Model formulation. *International Journal of Heat and Mass Transfer* 1987; **30**: 2161-2170.
7. Bennon WD, Incropera FP. A continuum model for momentum, heat and species transport in binary solid-liquid phase change systems. II. Application to solidification in a rectangular cavity. *Int. J. Heat Mass Transfer* 1987; **30**: 2171-2187.
8. Voller VR, Brent AD, Prakash C. The modeling of heat, mass and solute transport in solidification systems. *Int. J. Heat Mass Transfer* 1989; **32**: 1718-1731.
9. Beckermann C, Viskanta R. Double-diffusive convection during dendritic solidification of a binary mixture. *PhysicoChemical Hydrodynamics* 1988; **10**: 195-213.
10. Prakash C. Two phase model for binary solid-liquid phase change. Part I: Governing equations. *Numer. Heat Transfer B* 1990; **18**: 131-145.
11. Ni J, Beckermann C. A volume-averaged two-phase model for transport phenomena during solidification. *Metall. Trans. B* 1990; **22**B: 349-361.
12. Prescott PJ, Incropera FP. Numerical simulation of a solidifying Pb-Sn Alloy : The effects of cooling rate on thermosolutal convection and macrosegregation. *Metallurgical Transactions B* 1991; **22**B: 529-540.
13. Prescott PJ, Incropera FP, Bennon WD. Modeling of dendritic solidification Systems: reassessment of the continuum momentum equation. *International Journal of Heat and Mass Transfer* 1991; **34**9: 2351-2359.
14. Prescott PJ, Incropera FP. Convective transport phenomenon and macrosegregation during solidification of a binary metal alloy-I. *ASME Journal of Heat Transfer* 1994; **116**: 735-741.
15. Incropera FP, Ni J. Extension of the continuum model for transport phenomenon occurring during metal alloy solidification-I. The conservation equations. *International journal of Heat and Mass transfer* 1995; **38**7: 1271-1284.
16. Incropera FP, Ni J. Extension of the continuum model for transport phenomenon occurring during metal alloy solidification-II. Microscopic considerations. *International Journal of Heat and Mass Transfer* 1995; **38**7: 1285-1296.
17. Hughes TJR, Liu WK, Brooks A. Finite element analysis of incompressible viscous flows by the penalty function. *Journal of Computational Physics* 1979; **30** 1: 1-60.
18. Ganesan S, Poirier DR. Conservation of mass and momentum for the flow of interdendritic liquid during solidification. *Metallurgical Transactions B* 1990; **21**B: 173-181.
19. Felicelli SD, Heinrich JC, Poirier DR. Macrosegregation patterns in multicomponent Ni-base alloys. *Journal of Crystal Growth* 1997; **177**(1-2): 145-161.
20. Chorin AJ. Numerical solution of the Navier-Stokes equations. *Math. Comput.* 1968; **22**: 745-762.
21. Nithiarasu P, Seetharamu KN, Sundararajan T. Double diffusive natural convection in an enclosure filled with fluid-saturated porous medium: a generalized non-Darcy approach. *International Communications in Heat and Mass Transfer* 1997; **24**: 1121-1130.
22. Nithiarasu P, Seetharamu KN, Sundararajan T. Natural convective heat transfer in an enclosure filled with fluid saturated variable porosity medium. *Int. J. Heat Mass Transfer* 1997; **40**: 3955-3967.
23. Tezduyar TE, Mittal S, Ray SE, Shih R. Incompressible flow computations with stabilized bilinear and linear equal-order-interpolation velocity pressure elements. *Comput. Methods Appl. Mech. Engrg.* 1992; **95**: 221-242.

24. Tezduyar TE. Stabilized finite element formulations for incompressible flow computations. *Adv. Appl. Mech.* 1992; **28**: 1-43.
25. Tezduyar TE, Osawa Y. Finite element stabilization parameters computed from element matrices and vectors. *Computer Methods in Applied Mechanics and Engineering* 2000; **190**: 411-430.
26. Masud A, Hughes TJR. A stabilized mixed finite element method for Darcy flow. *Comput. Methods Appl. Mech. Engrg.* 2002; **191**: 4341-4370.
27. Drew DA. Mathematical modeling of two-phase flow. *Ann. Rev. Fluid Mech.* 1983; **15**: 261-291.
28. Ishii M. *Thermo-fluid dynamic theory of two-phase flow* (1st edn). Eyrolles: Paris, 1975.
29. Gray WG. Brief communication: local volume averaging of multiphase systems using a non-constant averaging volume. Int. J. Multiphase Flow 1983; **9** (6): 755-761.
30. Gray WG. A deviation of the equations for multi-phase transport. *Chem. Engng. Sci.* 1975; **30**: 229-233.
31. Whitaker S. Diffusion and dispersion in porous media. *A.I.Ch.E.* 1967; **13**: 420-427.
32. Poirier DR, Nandapurkar P, Ganesan S. The energy and solute conservation equations for dendritic solidification. *Metall. Trans. B* 1990; **22**B 889-900.
33. Beckermann C, Viskanta R. Mathematical modeling of transport phenomena during alloy solidification. *Appl. Mech. Rev.* 1993; **46**(1): 321-336.
34. Bousquet-Melou P, Goyeau B, Quintard M, Fichot F, Gobin D. Average momentum equation for interdendritic flow in a solidifying columnar mushy zone. *International Journal of Heat and Mass Transfer* 2002; **45** 3651-3665.
35. Poirier DR. Permeability for flow of interdendritic liquid in columnar dendritic alloys. *Metall. Trans. B* 1987; **18**B: 245-256.
36. Hughes TJR, Franca LP, Hullbert GM. A new finite element formulation for computational fluid dynamics: VIII. The Galerkin/least-squares method for advective-diffusive equations. *Computer Methods in Applied Mechanics and Engineering* 1989; **73**: 173-189.
37. Hughes TJR, Franca LP, Balestra M. A new finite element formulation for computational fluid dynamics: V. Circumventing the Babuska-Brezzi condition: A stable Petrov-Galerkin formulation of the Stokes problem accommodating equal-order interpolations. *Computer Methods in Applied Mechanics and Engineering* 1986; **59**: 85-99.
38. Hughes TJR, Franca LP. A new finite element formulation for computational fluid dynamics: VII. The Stokes problem with various well posed boundary conditions: Symmetric formulations hat converge for all velocity/pressure spaces. *Computer Methods in Applied Mechanics and Engineering* 1986; **65**: 86-96.
39. Franca LP, Hughes TJR and Stenberg S. Stabilized finite element methods for Stokes problem. In *Incompressible Computational Fluid Dynamics,* Gunzburger MD, Nicolaides RA (eds). Cambridge University Press: Cambridge, 1993; 87–107.
40. Illinca F, Hetu JF, Pelletier D. On stabilized finite element formulations for incompressible advective-diffusive transport and fluid flow problems. *Computer Methods in Applied Mechanics and Engineering* 2000; **188**: 235-255.
41. Hughes TJR. Multiscale phenomena: Green's functions, the Dirichlet-to-Newmann formulation, subgrid scale models, bubbles and the origins of stabilized methods. *Computer Methods in Applied Mechanics and Engineering* 1995; **127**: 387-481.
42. Amiez G, Gremaud P. On a numerical approach to Stefan-like problems. *Numer. Math.* 1991; **59**: 71-89.
43. Neilson DG, Incropera FP. Experimental study of unidirectional solidification of aqueous ammonium chloride in a cylindrical mold with and without rotation. *Exp. Heat Transfer* 1993; **6**: 131–155.